SANDIA REPORT
SAND2021-9640
Printed August 2021

Sandia National Laboratories

Spontaneous Imbibition Tests and Parameter Estimation in Volcanic Tuff

Kristopher L. Kuhlman, Melissa M. Mills, Jason E. Heath,
Matthew J. Paul, Jennifer E. Wilson, & J. Eric Bower

Prepared by
Sandia National Laboratories
Albuquerque, New Mexico
87185 and Livermore,
California 94550

Issued by Sandia National Laboratories, operated for the United States Department of Energy by National Technology & Engineering Solutions of Sandia, LLC.

Available to DOE and DOE contractors from
U.S. Department of Energy
Office of Scientific and Technical Information
P.O. Box 62
Oak Ridge, TN 37831

Telephone: (865) 576-8401
Facsimile: (865) 576-5728
E-Mail: reports@osti.gov
Online ordering: http://www.osti.gov/scitech

Available to the public from
U.S. Department of Commerce
National Technical Information Service
5301 Shawnee Rd
Alexandria, VA 22312

Telephone: (800) 553-6847
Facsimile: (703) 605-6900
E-Mail: orders@ntis.gov
Online order: https://classic.ntis.gov/help/order-methods/

ABSTRACT

We present a dynamic laboratory spontaneous imbibition test and interpretation method, demonstrated on volcanic tuff samples from the Nevada National Security Site. The method includes numerical inverse modeling to quantify uncertainty of estimated two-phase fluid flow properties. As opposed to other approaches requiring multiple different laboratory instruments, the dynamic imbibition method simultaneously estimates capillary pressure and relative permeability from one test apparatus.

ACKNOWLEDGEMENTS

This research was funded by the National Nuclear Security Administration, Defense Nuclear Nonproliferation Research and Development. The authors acknowledge important interdisciplinary collaboration with scientists and engineers from Los Alamos National Laboratory, Lawrence Livermore National Laboratory, Mission Support and Test Services, Pacific Northwest National Laboratory, and Sandia National Laboratories (SNL).

The authors thank Scott Broome of SNL for supervising the work and providing the samples from the Underground Nuclear Explosion Signatures Experiment project.

The authors thank Tara LaForce of SNL for technically reviewing the report.

CONTENTS

LIST OF FIGURES

LIST OF TABLES

ACRONYMS AND DEFINITIONS

Abbreviation	Definition
2D	two-dimensional
3D	three-dimensional
DREAM	differential evolution adaptive Metropolis
EDS	energy dispersive spectroscopy
MCMC	Markov chain Monte Carlo
NNSS	Nevada National Security Site
PFLOTRAN	parallel flow and transport (www.pflotran.org)
UNESE	Underground Nuclear Explosion Signatures Experiment
SEM	scanning electron microscopy
tiff	tagged image file format
VISA	virtual instrument software architecture
XRCT	X-ray computed tomography

1. INTRODUCTION

Two-phase fluid flow of water and gas is important in many applications in diverse rock types, including gas migration through the vadose zone associated with an underground nuclear explosion (Heath et al., 2021). At the porous medium scale, the main two-phase fluid flow nonlinear relationships are

1. the moisture retention curve, which is the relationship between relative water saturation (i.e., the fraction of pore volume filled with water; Figure 1) and the potential energy of water as affected by capillary pressure and adsorptive forces; and
2. the relative permeability curve, which is the relationship between water saturation and the liquid relative permeability (i.e., the fraction of the intrinsic permeability at less than full fluid saturation) or the gas relative permeability.

These non-linear relationships or "curves" are typically parameterized by fitting simple functional forms to laboratory data collected from static tests for capillary pressure—parameters derived from fitting capillary pressure are then often used to blindly predict the relative permeability curves (Priesack & Durner, 2006; Heath et al., 2021).

Here we present relatively simple dynamic (i.e., transient) spontaneous imbibition laboratory testing method. We demonstrate the method on volcanic tuffs and fit models to these test data using Markov chain Monte Carlo (MCMC) Bayesian methods. The dynamic tests provide indirect information about the moisture retention and relative permeability curves, which are obtained through parameter estimation. Compared to static testing methods (Figure 1), dynamic imbibition tests require inverse modeling (i.e., parameter estimation) where a numerical model or analytical solution is compared to observations. The imbibition laboratory data do not directly measure moisture retention and relative permeability, but we contend the data do adequately constrain the model parameters through the inverse numerical modeling process.

Usually, two-phase fluid flow properties are estimated from static tests, where either a wetting (e.g., water) or non-wetting (e.g., mercury) fluid is drawn into a sample at different steps of capillary pressure (e.g., Sahimi, 2011). Each static step of the process produces a single saturation vs. capillary pressure data point. When taken together these points delineate a moisture retention curve. Estimates of relative permeability at different levels of water saturation are found from different laboratory tests involving dynamic or steady-state fluid flow, which are not as commonly run as capillary pressure tests. Relative permeability is a much more complex measurement (i.e., several thousands of dollars per test). Mercury injection capillary pressure tests are common and inexpensive (i.e., a few hundred dollars per test), but are limited to small samples (i.e., approximately 1-inch core plugs), and may produce different results if the rocks have water-reactive components like clay or zeolite. When conducting static water-based capillary pressure tests, a suite of measurement methods may be needed to obtain the full moisture retention curve across the potentially large range of capillary pressures for a given sample (Figure 1; Tuller & Or, 2005).

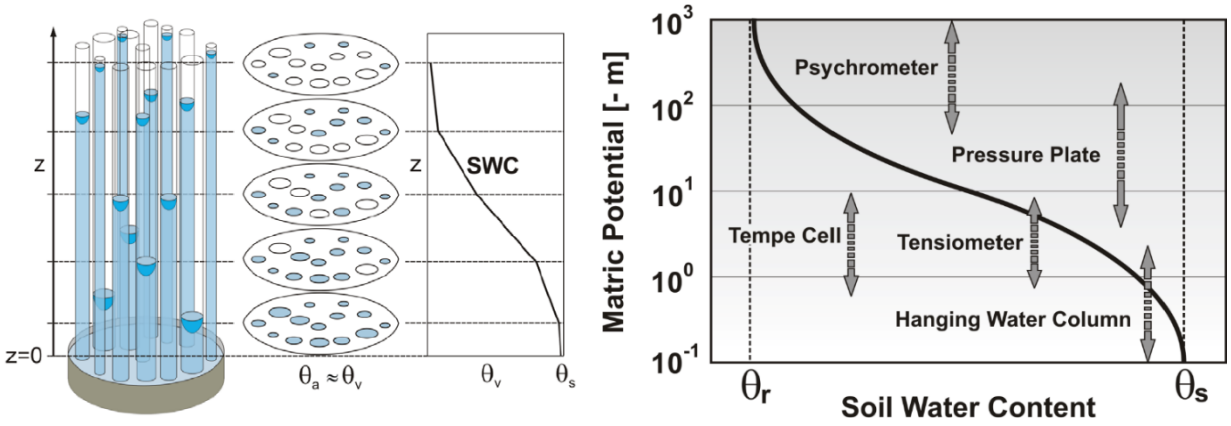

Figure 1. Conceptualization of the moisture retention curve as a bundle of capillary tubes (left) and approximate ranges of static laboratory measurement methods (right) (Tuller & Or, 2005). SWC is "soil water characteristic", another name for the moisture retention curve. The curve on the right is a SWC expressed with "Matric Potential," which is the potential energy of the water in the porous medium as affected by capillary and adsorptive forces. The x-axis variable θ is volume wetness, the ratio of the volume of water to the total volume of soil or rock in question.

Although static tests are common because they are trivial to interpret, there are some less popular transient laboratory methods for estimating moisture retention curve data (Dullien, 1992; Stephens, 1996; Hillel, 1998; Sahimi, 2011), including the instantaneous profile method, the Bruce-Klute method, the pressure-plate method, the one-step outflow method, and the centrifuge method. The instantaneous profile method involves applying a constant infiltration rate or water flux to one end a sample. The Bruce-Klute method involves imbibition into a horizontal column, followed by estimation of the moisture profile. The pressure-plate and one-step outflow methods involve draining the water out of a water-saturated sample through a porous ceramic plate via gas pressure applied in a sealed chamber. The centrifuge method rapidly drains water from a saturated sample via centrifugal forces. Out of the methods just listed, the historical Bruce-Klute spontaneous imbibition method is the most like the method proposed here, except instead of measuring the mass imbibed, they measure the volumetric flowrate of water produced at a constant head, and they measure saturation by sub-sampling and gravimetric water content measurements after the test (Bruce & Klute, 1956). The Bruce-Klute laboratory data were traditionally not used to estimate van Genuchten model parameters; the data were historically used to produce a table of hydraulic diffusivity (ratio of permeability and storage coefficient) values as a function of water content.

Spontaneous water imbibition is the process of water (or any wetting phase) being drawn into a relatively dry water-wetted porous material through capillary forces. We conduct spontaneous imbibition tests vertically against gravity (horizontal tests that do not include effects of gravity are also possible), and we do not apply any pressure to drive flow aside from the hydrostatic pressure associated with <1 cm of water in the reservoir into which the bottom-most portion of the core sample is placed (see Section 2.3, Laboratory Methods for Imbibition Tests).

The approach we take here was inspired by previous reports of imbibition tests in volcanic tuff (e.g., Peters et al., 1987; Kwicklis et al., 1998), to gather data to constrain two-phase fluid flow properties possibly relevant to m- and km-scale numerical models in volcanic tuff at what is now the Nevada National Security Site (NNSS). While parameter estimation has been used previously to quantify two-phase fluid flow properties from imbibition tests (e.g., Eaton & Bixler, 1987; Rasmussen et al., 1996), our approach is unique. We couple the use of an automated global parameter estimator (i.e.,

MCMC) to estimate the best-fit parameters and quantify the relative uncertainty of the model fit to the data. Our method also applies to whole core samples—in this case approximately 2.5 inches diameter and 6 to 8 inches in length—to sample a larger volume of tuff lithofacies to obtain more representative data (compared to 1-inch core plugs). Petrographic observations link the fluid flow properties to the underlying geologic controls (e.g., pore types and the arrangement of the mineral phases).

Analytical solutions or scaling approaches exist for multiple varieties of imbibition problems, with most of the solutions coming from the soil science or petroleum engineering literature (Li & Horne, 2006; Sahimi, 2011; Schmid et al., 2016). Although spontaneous imbibition solutions in the literature vary in the details of their treatment of the problem, they generally agree the infiltrated mass of water is proportional to the square root of time (Schmid & Geiger, 2012). Most analytical solutions for spontaneous imbibition assume infinitely long samples and a specific functional form for the moisture retention curve. Few solutions consider the effects of imbibition into irregular sample shapes (Zimmerman et al., 1990).

In this report, we use Bayesian MCMC methods to automatically adjust four key parameters in a PFLOTRAN simulation to match observations. Rather than using analytical solutions, this more general approach will eventually allow fitting of models using a range of capillary pressure curve constitutive models and there is a benefit to using the same numerical model to fit the data and make eventual predictions of large-scale fluid flow. Using numerical models in parameter estimation allows explicitly accounting for irregular sample geometry, physically realistic equations of state for water or pore compressibility, or non-ideal boundary conditions if necessary (e.g., short samples with end-effects are still useful because estimates of the relevant fluid flow parameters can be obtained).

2. METHODS

2.1. Rock Samples and Geologic Characterization

Rock samples were obtained from core holes at the NNSS in the Underground Nuclear Explosion Signatures Experiment (UNESE) test bed (Heath et al., 2020; 2021). Lithologic characterization is performed by two- and three-dimensional (2D and 3D) petrography using thin sections and X-ray computed tomography (XRCT).

Two standard petrographic thin sections, 27 × 46 mm and 30 μm in thickness, were made from the rock samples, including one parallel and one perpendicular to the core axis. These thin section rock samples are not the same samples used in the imbibition tests but are from similar lithologies. Microtexture and pore morphologies were observed and imaged on a Leitz Wetzlar Orthoplan-Pol Petrographic Microscope using a Leica DMC 5400 camera and LASX imaging software. Scanning electron microscopy (SEM) was performed using a TESCAN Vega3 instrument. Thin sections were coated with gold-palladium alloy using a Denton Vacuum Desk IV sputter-coater. Microtexture of each thin section was observed and imaged using backscattered electrons and secondary electrons in high-vacuum mode at an accelerating voltage of 20 kV. Elemental composition from select portions of each thin section (pore-lining minerals) was obtained using an EDAX energy-dispersive X-ray spectroscopy (EDS) system at an accelerating voltage of 15 kV. The EDS spectra were collected and analyzed using the TEAM EDS analysis system for the SEM. Key petrographic observations of pore structure that affect fluid flow include the following: solid phases lining pores or fractures; size, shape, and connectivity of pores or fractures; and mineralogy.

A North Star Imaging X50 micro-CT scanner with a PaxScan 2520DX Digital Image detector were used to obtain XRCT data on four rock samples prior to their use in imbibition tests. The XRCT image acquisition and reconstruction were performed with North Star efX-DR and efX-CT software, respectively. This produced registered tomographic reconstructions as 16-bit tiff (tagged image file format) image stacks. Visualization and post-processing of XRCT data sets were performed using the Fiji distribution (Schindelin et al., 2012) of ImageJ version 1.53k and the Thermo Fisher software Avizo version 2020.2. The 16-bit tiff image stacks were converted to 8-bit tiff image stacks with Fiji, which were imported into Avizo for 2D and 3D rendering for qualitative interpretation of the core-scale lithologic textures and visualization of vertical connectivity of the constituent phases in the direction of water imbibition into the samples. A workflow for volumetric quantification of sample constituents was developed and applied to one of the rock samples (i.e., Sample 3 or UE-12p#7 56.2-57.0). The workflow involved masking to the outside of the sample with marker-based watershed techniques in Avizo, followed by correction for beam hardening using an ImageJ plugin (Romano et al., 2019) with GPU-acceleration (Haase et al., 2020), and then subsequent steps in Avizo including marker-based segmentation and volume fraction calculation for the dominant constituent phases of the sample, with 2D and 3D visualization of those phases.

2.2. Governing Equations

We use PFLOTRAN (Hammond et al., 2014) to numerically solve the spontaneous imbibition flow problem. PFLOTRAN is an open-source, state-of-the-art, massively parallel subsurface flow and reactive transport simulator. We assume flow of water into oven-dry porous media samples is described by Richards' equation for variably saturated flow (Richards, 1931; Lichtner et al., 2021)

$$\frac{\partial}{\partial t}(n\, S_\ell\, \rho) = -\nabla \cdot (\rho \bar{q}), \tag{1}$$

where n is dimensionless porosity, S_ℓ the dimensionless liquid degree of saturation, ρ is the liquid density [$\mathrm{kg/m^3}$], and $\bar{q}$ is the Darcy velocity [$\mathrm{m/s}$], given as

$$\bar{q} = -\frac{k k_{rw}(S_\ell)}{\mu} \nabla(p_l - \rho g z), \tag{2}$$

where k is intrinsic permeability [$\mathrm{m^2}$], k_{rw} is the dimensionless relative permeability to water, μ is water viscosity [$\mathrm{Pa \cdot s}$], g is the gravitational acceleration [$\mathrm{m/s^2}$], and z is the positive-up vertical coordinate [m].

Frequently, porous media samples exhibit a property known as residual or irreducible saturation, S_r (the equivalent irreducible volume wetness θ_r is shown in Figure 1, where $\theta_r = S_r n$). At this degree of saturation or lower, capillary effects dominate and retained water cannot be removed by ordinary draining techniques. Below this point, few pores are hydraulically connected, and the relative permeability is negligible. Typically liquid saturation above the residual is of concern, van Genuchten (1980), and others use the concept of an effective saturation, S_e, which is normalized over the span from residual to saturation (saturation in terms of volume wetness θ_s is shown in Figure 1; the span of residual to full saturation in volume wetness is shown by the vertical dotted lines in Figure 1), that is

$$S_e(S_l) = \frac{S_l - S_r}{1 - S_r}. \tag{3}$$

The corresponding van Genuchten (1980) moisture retention curve, expressing effective saturation as a function of capillary pressure, is

$$S_e(p_c) = \left[1 + (\alpha p_c)^{\frac{1}{1-m}}\right]^{-m}, \tag{4}$$

where m is the dimensionless van Genuchten shape parameter and α is the van Genuchten capillary pressure scaling factor [$1/\mathrm{Pa}$]; $1/\alpha$ is often called the air-entry pressure. Van Genuchten also noted that this saturation function can be analytically integrated in the Mualem relative permeability model, yielding the closed-form model for wetting-phase relative permeability

$$k_{rw}^M(S_e) = \sqrt{S_e}\left[1 - (1 - {S_e}^{1/m})^m\right]^2, \tag{5}$$

where the superscript M designates the Mualem relative permeability model. To convert Richards' equation (1) to a form solely in terms of liquid pressure, p_l, (the left-hand side is in terms of liquid saturation), we substitute equation (2) into (1) and substitute the derivative of equation (4) with respect to p_c (called capacitance, C; Klavetter & Peters, 1986; Warrick, 2003),

$$C(p_c) \equiv \frac{\mathrm{d}S_\ell}{\mathrm{d}p_c} = \frac{\mathrm{d}S_\ell}{\mathrm{d}S_e} \cdot \frac{\mathrm{d}S_e}{\mathrm{d}p_c} = (1 - S_r)\frac{\mathrm{d}S_e}{\mathrm{d}p_c} \tag{7}$$

into equation (1), resulting in

$$-C(p_c)\frac{\partial}{\partial t}(p_l\, n\, \rho) = \frac{k k_{rw}(S_e(p_c))}{\mu}\left(\nabla^2 p_l - \rho g \frac{\partial k}{\partial z}\right), \tag{8}$$

where the negative on the left-hand side comes from $\mathrm{d}p_l/\mathrm{d}p_c$. The time derivatives of porosity and density on the left-hand side manifest in numerical models as formation compressibility ($\partial n/\partial t$) and the equation of state for the density of water ($\partial \rho/\partial t$).

Notably, in the liquid pressure form of Richards' equation (1) the relative permeability curve appears on the right-hand side (in green) associated with the spatial variability and the derivative of the moisture retention curve appears on the left-hand side (in red) with the temporal variability. Richards' equation is strongly non-linear because of these two terms that each depend on capillary pressure. We lay out these equations to explicitly make this point because equation (8) is the governing equation that shows how fluid flow through the sample is impacted by both the moisture retention curve and the relative permeability curve, which are related but are not identical. Thus, fitting this governing equation (8) to both temporal and spatial observations can be used to simultaneously obtain parameter estimates of moisture retention and relative permeability from dynamic imbibition laboratory tests that involve both capillary forces and the competing flow of air and water in the porous medium.

The Mualem (1976) approach was used above to derive a closed-form expression for relative permeability (equation 5) from the moisture retention curve, but another approach is also implemented in PFLOTRAN for the van Genuchten model. For comparison, the Burdine (1953) relative permeability relationship for the van Genuchten model is

$$k_{rw}^{B}(S_e) = {S_e}^2\left[1 - (1 - {S_e}^{1/m})^m\right], \tag{9}$$

where the superscript B designates Burdine. In Section 4.4 parameter estimation is done on Sample 1 with this model to quantify the effects this model choice has on both the capillary pressure curve and the relative permeability curve. In the PFLOTRAN implementation used here, both k_{rw}^{B} and k_{rw}^{M} use the same S_e formulation. From static capillary pressure tests the moisture retention curve alone is parameterized, and the relative permeability is predicted blindly (assuming either the Mualem or Burdine relationship). Our test interpretation method allows considering both curves and their effects on the model predictions simultaneously.

The left panel in Figure 2 shows the van Genuchten moisture retention function (equation 4) for several m (line color) and α (dashed vs. solid) values. The right panel compares the Mualem (equation 5) and Burdine (equation 9) relative permeability models (thick vs. thin lines) for a range of m values (α does not directly impact k_{rw}). The Mualem model predicts a wider variability in k_{rw}^{M} given a range of m, compared to k_{rw}^{B} at a given value of S_e.

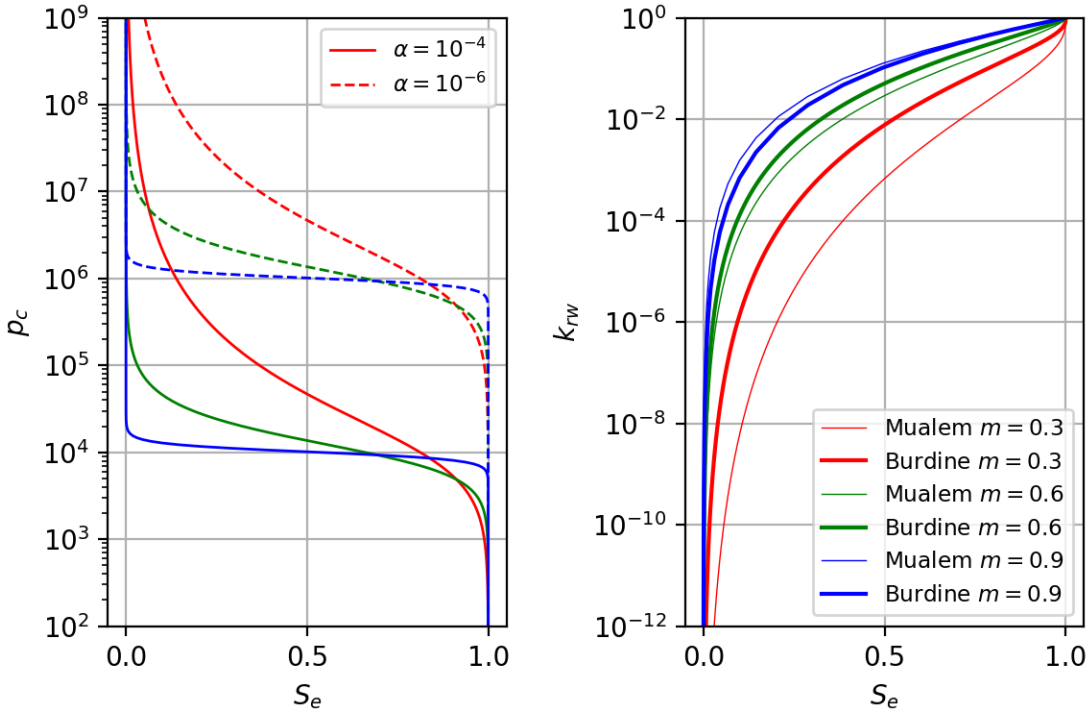

Figure 2. Illustration of van Genuchten model for several parameters (left), and comparison between Mualem and Burdine relative permeability models (right).

Lastly, the Young-Laplace equation (e.g., Adamson & Gast, 1997) can be used to relate a characteristic capillary pressure to a characteristic pore size

$$a = \frac{2\,\sigma\cos\theta}{p_c}, \tag{10}$$

where a is a characteristic pore radius [m], σ is the surface tension of water [72 mN/m], and θ is the liquid-solid-rock contact angle (here assumed to be zero—fully wetting—for simplicity). For this water-air system, the relationship can be given as $a = 0.144\,\alpha$, when α is given in $1/\mathrm{Pa}$ and a is given in m. The air-entry pressure ($1/\alpha$) is associated with the first excursion of air into a water saturated sample, so it would likewise be associated with the largest pores in a sample. Drainage tests would likely provide better estimates of air-entry pressure than imbibition tests. The smallest pore size in a sample, associated with the capillary pressure that water first imbibes (i.e., a water-entry pressure), would be more relevant to imbibition tests.

2.3. Laboratory Methods for Imbibition Tests

The goal of the testing approach was to create a simple laboratory setup with the possibility of realistically constraining two-phase fluid flow parameters. Previous spontaneous imbibition approaches we found in the literature focused on monitoring the change in sample weight after it was placed in a shallow pool of water (Peters et al., 1987). However, this required removing the sample each time to weigh, disrupting the imbibition process and creating potential mass errors. The method used here monitors the weight change of a Mariotte bottle (with no handling disturbance to the sample during the test), which provided a constant flow of fluid to the sample reservoir. The following describes this setup, along with additional sample details.

2.3.1. Sample Preparation and Experimental Setup

The selected core samples were placed "as received" (e.g., no additional cutting) into a forced convection oven at 60 ºC for at least 72 hours to ensure uniformly dry starting conditions, without removing structural water from hydrous mineral phases like zeolite. The before and after weights were recorded (Table 1) along with additional dimensional measurements.

Table 1. Sample dimensions and initial weights.

Sample	Diameter [in]	Length [in]	Initial weight [g]	Dry weight [g]
1	2.3125	7.25-7.5	812.09	805.72
2	2.375	8.1	1039.91	1001.24
3	2.375	7.875-8.125	752.50	735.22
4	2.375	6.25-6.75	651.83	649.46

The experimental setup is shown in Figure 3. It consisted of a sample holder/reservoir, Mariotte bottle, and balance. A clear, Lexan column was chosen as the sample holder for visibility of water levels, ensuring sealed tubing connections, and reduced air circulation surrounding samples (to minimize evaporation). To maintain a constant flow of fluid to the sample reservoir, a Mariotte bottle was assembled from a Fleaker with a two-hole rubber stopper and two sizes of tubing. The bottle maintains pressure head in the reservoir at the elevation of the end of the air inlet tube. If there is a decrease in the reservoir fluid level, fluid will begin to flow from the bottle, maintaining the fluid level in the reservoir available for the sample to imbibe. Both Ankeny (1988) and Constantz & Murphy (1987) showed the diameter of the bottle and sizes of tubing have direct effects on the flow to the reservoir. Mariotte bottles with smaller diameters improve measurement precision for low flow rates. Therefore, several configurations of the Mariotte bottle were tested by performing imbibition tests with sponges to improve the flow rate sensitivity. This consisted of changing tubing sizes of outflow and air inlet, as well as evaluating a smaller graduated cylinder and a vacuum Nalgene bottle.

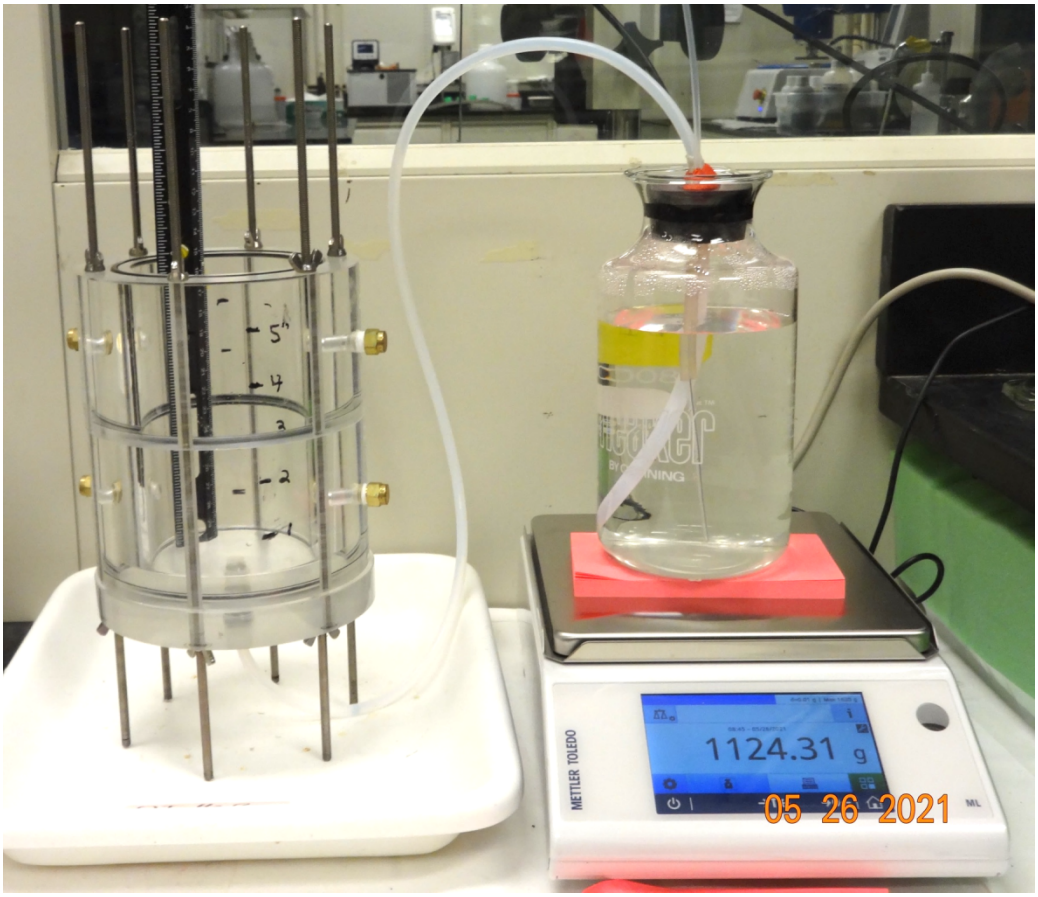

Figure 3. Setup of experiment with sample column, Mariotte bottle, and balance.

As expected, a smaller outflow tube resulted in a slower filling rate, but it was determined this could have negative implications on results if a sample had high uptake and the reservoir did not replenish fast enough. Instead, the use of a reduced diameter air inlet tube produced greater sensitivity to the pressure difference. The two other bottles tested could have made the system more sensitive, but it was more difficult to create a dependable seal at the mouth of these two bottles around the tubing. From these trials, the final setup was a 0.25-inch outflow tube, 0.125-inch air inlet tube, and a 3.5-inch diameter Fleaker with an adequate two-hole rubber stopper.

To monitor the amount of fluid imbibed by the sample, the Mariotte bottle was placed on a balance connected to a computer for automated data collection. A Python script was used to acquire mass and time data every second once the experiment started using PyVISA for instrument communication, a Python wrapper around the VISA (virtual instrument software architecture) library. The script saves the data into an Excel file for easy exporting and visualization of the imbibition response.

In addition to mass data collection, the wetting front of the fluid was monitored by imaging (i.e., photographing with a digital still or video camera while recording the time) the sample during the experiment. Using the inch measurement lines marked on the column, the level of the wetting front was associated with an elapsed time, quantifying the location of the wetting front during the test.

2.4. Modeling Methods

2.4.1. PFLOTRAN Imbibition Model

PFLOTRAN (Hammond et al., 2014) was used to simulate the laboratory imbibition experiment. We used RICHARDS flow mode, which solves Richards' variably saturated flow equation and therefore does not explicitly track the migration of the gas phase, as a two-phase flow solution does. This is a reasonable approximation that saves computational effort (Richards' equation involves liquid pressure, while explicit two-phase simulations involve liquid and gas pressure, and a relative saturation), since mobility (i.e., the ratio of permeability to fluid viscosity) of air is much higher than the mobility of water and the samples are open to the atmosphere, allowing gas to escape freely as water imbibes. A one-dimensional solution mesh (200 elements representing the vertical extent of the sample) was created with the same dimensions as the laboratory sample. The simulation had an initial condition representative of oven-dry conditions (capillary pressure of 10 MPa) and a bottom boundary condition representative of the reservoir (hydrostatic pressure of 101325 Pa, assigned at a datum set equal to the depth of water in the sample holder, e.g., 0.82 cm).

The simulation was run for the duration of the lab experiment, with the model saving observations of total mass of water flowing in through the boundary condition and observations of liquid saturation at different elevations. The model mass balance predictions of inflow at the model lower boundary were compared to laboratory observations of water imbibed. The model predictions of liquid saturation through time at observation locations were post-processed by a Python script to estimate the time associated with the arrival of a wetting front (assumed the time when 50% saturation is first reached) at each observation location. The model predictions of wetting-front arrival time at specified vertical locations were compared to observations of wetting front position during the experiment, documented by photographs and video.

2.4.2. Parameter Estimation via DREAM

The DiffeRential Evolution Adaptive Metropolis (DREAM) Markov chain Monte Carlo (MCMC) global Bayesian parameter estimation framework (Vrugt et al., 2009; Vrugt, 2016) was used to estimate distributions of parameters by minimizing model/data misfit. Four parameters were estimated in each test, with relatively wide minimum and maximum parameter ranges:

- intrinsic (saturated) permeability [m^2] 10^{-18} to 10^{-12}
- total porosity [fraction] 0.20 to 0.50
- van Genuchten α [1/Pa] 10^{-6} to $10^{-2.5}$
- van Genuchten m [dimensionless] 0.3 to 0.99

The observed mass of water imbibed (i.e., loss of mass from the Mariotte bottle) through time was re-sampled to a uniform spacing in logarithmic space (data were originally collected approximately every second), and the observations of the wetting front elevation and elapsed time were used as inputs. The wetting-front observations were weighted less ($1/60$) than the mass-imbibed data (unit weight), since they were different units and numerically much larger.

At the beginning of each test, when the dry sample is placed into the sample holder with an initial level of water (~1 cm), the water level in the sample container rises. This is due to displacement of water by the solid sample. The volume displaced is computed as the cross-sectional area of the sample, times the initial depth of the water, times the sample solid fraction ($1 - n$). The fixed gas

pressure of the head space in Mariotte bottle prevents water from flowing back into the Mariotte bottle (i.e., like a one-way valve), so no water flows into the sample holder from the bottle until the water associated with the displacement has imbibed into the sample, lowering the reservoir level below the end of the air intake in the Mariotte bottle. This was handled in the simulations by computing the displaced mass of water from the sample geometry, subtracting this amount from the model-predicted mass imbibed and setting all negative mass-imbibed values to zero.

The parameters were given wide but physically realistic parameter ranges, with uniform initial distributions determined through Latin hypercube sampling across their ranges, rather than through covariance or prior distributions. The saturated (i.e., intrinsic) permeability and the van Genuchten α were both log-transformed (base 10) during the parameter estimation process. Some combinations of parameters lead to either very long model run times or failure of the simulation to converge. The longest runtimes were associated with large m (e.g., > 0.8) and large α parameters (e.g., > 0.001). Both parameters lead to potentially very large capillary pressures at low water saturations, which can lead to very small time-steps, based on the poor convergence of the Newton solver in PFLOTRAN.

Using the new loop_invariant van Genuchten implementation (Nole et al., 2021) sped up execution times significantly in two ways. First, the loop_invariant approach works to cache many intermediate values used in the calculation of the capillary pressure and relative permeability (computed at initialization), to speed up the overall execution of the model. The capillary pressure functions are called for each model element, for each linear solve, multiple times at each Newton iteration, at each time step, so even small optimizations can save significant overhead (e.g., a few percent speedup) in a variably saturated flow simulation.

Secondly, the loop_invariant addition includes an extension of the van Genuchten model to water saturations below residual saturation. Traditionally, the derivative of the capillary pressure with respect to water saturation becomes infinite (i.e., a vertical line) at the residual saturation. Below the residual, the effective saturation is ill-defined. In previous versions of PFLOTRAN, the capillary pressure was truncated to a designable, but constant maximum capillary pressure (the default value was 1 GPa). Where the flat maximum capillary pressure intersects the ordinary van Genuchten curve, there is a large discontinuity in the derivative, that leads to numerical instability in Newton's method. Consequently, starting the simulation at or below residual saturation can be numerically unstable, even if the spontaneous imbibition test should only ultimately lead to wetter conditions than residual saturation during the simulation. Perturbations in the saturation during Newton iterations can lead to very large changes in the capillary pressure, which may result in the automatic time-stepping algorithm taking smaller timesteps, due to less-than-optimal convergence.

Various models have been proposed to resolve this discontinuity and model capillary pressure below the residual. The options discussed in Sun et al. (2010) were recently implemented in PFLOTRAN (Nole et al., 2021). Here, we used the exponential unsaturated extension, which provides a continuity in capillary pressure and its derivative from residual saturation over to zero saturation. Aside from numerical advantages, the exponential approach has previously shown good agreement with experimental data (Webb, 2000). Even if the simulation does not include these very dry conditions, by avoiding the discontinuity in the capillary pressure derivative improves the numerical stability of the model, allowing larger time steps.

3. RESULTS

3.1. Sample 1

Sample 1 is UNESE core sample UE-12p#4 644.2-644.8. As based on thin section observations (Figure 4), Sample 1 is a vitric nonwelded tuff, composed of unflattened and glassy pumice with preserved vesicles, phenocrysts of quartz and feldspar, and lithic fragments in a matrix of ash and glass shards, with some smectite clay minerals from alteration of volcanic glass. The sample's microtexture contains fine-grained ash and smectite, which have small pores that are difficult to directly visualize in the petrographic images (Figure 4). Larger pores from pumice vesicles are clearly visible, but probably do not represent a connected large-scale pore network through the sample. The core-scale texture of sample is homogeneous and massive, with few larger components (likely pumice clasts) visible in the XRCT images (Figure 5). The fine-grained matrix (i.e., volcanic ash and smectite) is the component of the sample that dominates connectivity in the vertical direction of imbibition. Large fractures are not visible.

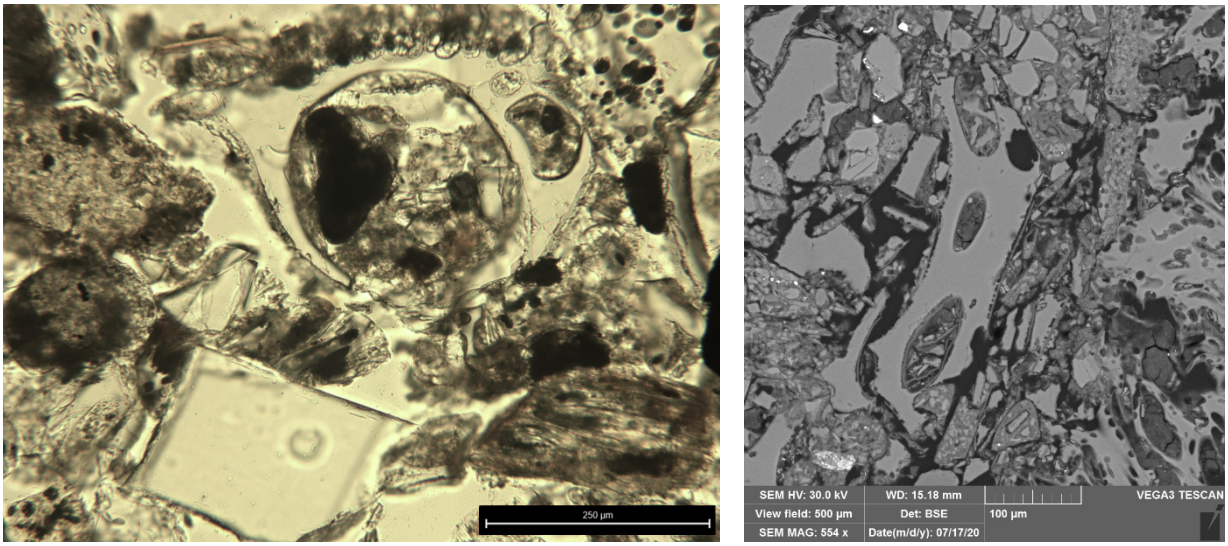

Figure 4. Petrographic image (left) and SEM image (right) showing microtexture of vitric nonwelded tuff representative of Sample 1, including preserved pumice vesicles, angular phenocrysts, and fine-grained matrix of volcanic ash and smectite.

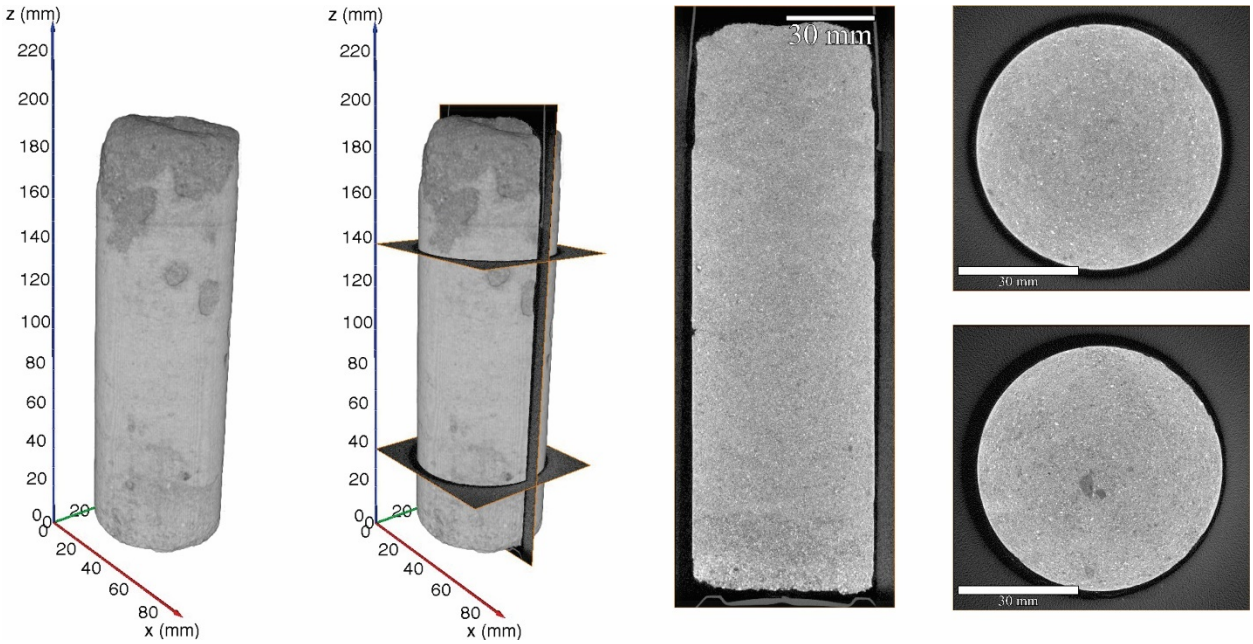

Figure 5. X-Ray CT image montage for Sample 1. Voxel resolution of the XRCT data set is 35.8 µm, with resolvable feature size of approximately 107 µm. 3D rendering on left shows positions of cross-sections on right, with the upper horizontal plane corresponding to the image on the upper right. Larger features visible in the X-Ray CT reconstruction (left) are core surface features, and cross-sections show only fine-grained matrix material (volcanic ash and smectite).

3.1.1. Laboratory Data

The raw and resampled mass imbibed data are shown in Figure 6. The black dots represent the data saved by the Python script, at approximately 1 second intervals. The red squares are mean values in intervals located uniformly in log (base 10) time. A set of 100 intervals were chosen between the first and last observation, while only 82 average data were exported because some of the early intervals did not include a data point.

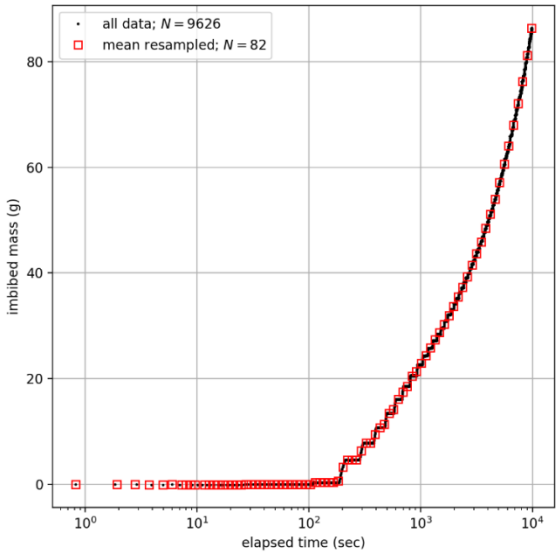

Figure 6. Observed (black dots) and resampled (red squares) data from Sample 1.

Wetting front observations taken from still photos used in the calibration are listed in Table 2. Figure 7 shows photos of the wetting front during the test—a plastic bag was put over the sample holder to minimize evaporation (some minor raveling occurred at the end of the sample placed in the water). The average wetting front velocity computed from adjacent wetting front observations is 1.87×10^{-5} m/s.

Table 2. Wetting front observations for Sample 1.

Observation Time [min:sec]	Elapsed Time [sec]	Wetting Front Height [m]
4:00	240	0.027
10:00	600	0.043
60:00	3,600	0.103
80:00	4,800	0.111
95:00	5,700	0.119
100:00	6,000	0.123

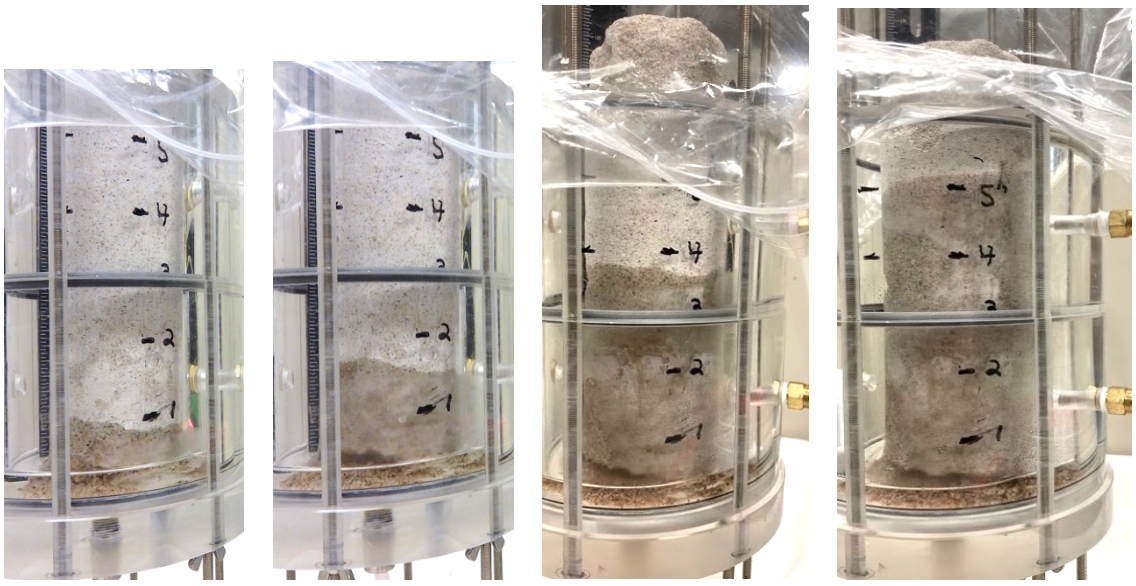

2 minutes 10 minutes 50 minutes 100 minutes

Figure 7. Images of the wetting front moving through Sample 1 over time. Numbers on the sample holder indicate inches from bottom.

3.1.2. Model Fit to Data

DREAM was used to simultaneously fit the model-predicted mass imbibed and wetting-front elevation to the observed data. The progress and convergence of the MCMC chains is shown in Figure 8; each of the three chains is a different color line. The first 2,000 iterations per chain were considered a burn-in period, while a total of 50,050 iterations were completed across all three chains (16,650 iterations per chain).

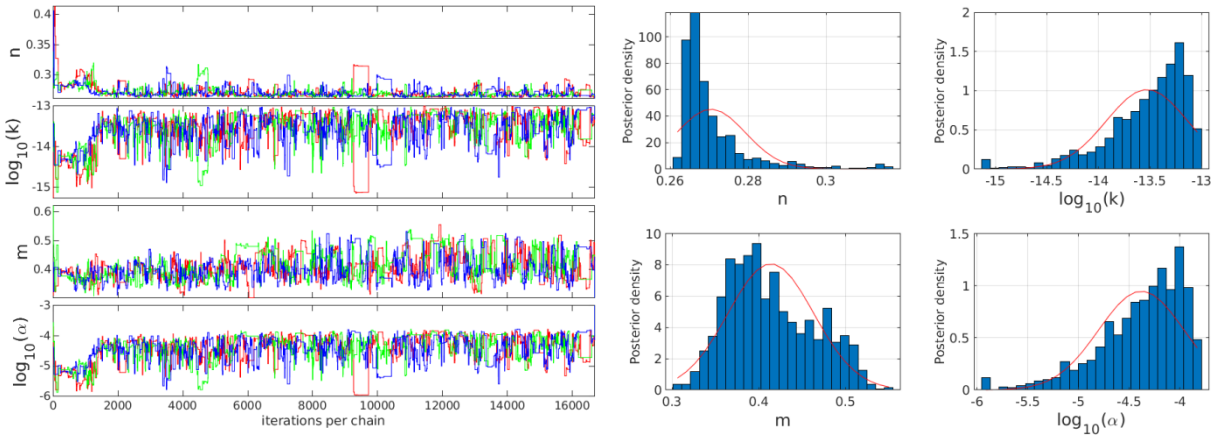

Figure 8. Convergence plot (left) showing evolution of chains for Sample 1. Histograms of chains (right) shown with best-fit Gaussians in red.

The chains (less their burn-in period) are plotted as histograms in Figure 8. The red lines are Gaussian distributions with the same mean and variance as the distribution, used to visually quantify a sense of skewness or non-normality in the posterior distributions. Table 3 summarizes the mean, variance, and the mode for each parameter. The mode is the tallest bar in the histogram. For very skew distributions, the mode is a better estimate of the "most likely value" than the mean.

Table 3. Statistics on posterior distribution for Sample 1.

Parameter [units]	Mean	Variance	Mode
Porosity (n) [-]	0.270	7.80×10^{-5}	0.266
Permeability (k) [m^2]	$10^{-13.53}$	1.54×10^{-1}	$10^{-13.21}$
van Genuchten m [-]	0.414	2.45×10^{-3}	0.398
van Genuchten α [1/Pa]	$10^{-4.38}$	1.65×10^{-3}	$10^{-4.00}$

Relating $\alpha = 10^{-4}$ to a pore size using equation (10) results in a characteristic pore radius size for this sample of 14 μm. This is comparable to microscopic observations in Figure 4.

Figure 9 shows pairwise 2D scatter plots of the posterior distribution. The diagonals of the matrix are the same histograms shown in Figure 8, while the off-diagonal plots (upper and lower triangles are the transposed) approximate two-dimensional histograms with color-coded gridded contour plots of density. Orange and yellow colors indicate a high posterior density, dark blues indicate a low posterior density, and white indicates no samples. Each off-diagonal 2D histogram has a different color scale, but high is always yellow and low is always blue. The values of peaks can be inferred from the histograms, which are also shown in Figure 8.

Strong positive correlations are seen between $\log_{10}(\alpha)$ and $\log_{10}(k)$, and weaker positive correlations are seen between $\log_{10}(\alpha)$ and m and between $\log_{10}(k)$ and m. Negative correlations are seen between n and all other parameters. The red lines in Figure 9 are linear best fits, quickly illustrating the sign of the slope or correlation.

These 2D histograms show complex non-linear correlations between some parameters, which are not captured in linearized gradient-based parameter estimation methods that only give a mean and a variance or 95% confidence interval. The posterior distributions from the MCMC method provide unique information about the model structure and its relationship to the data.

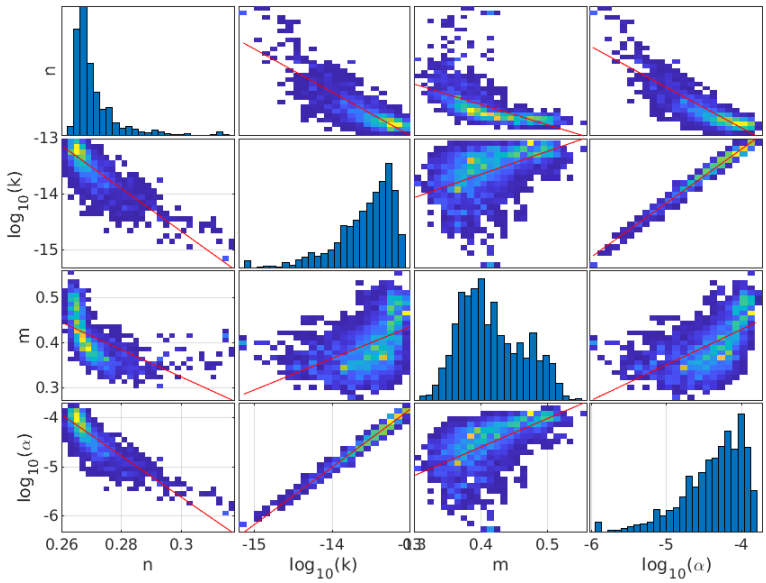

Figure 9. Pairwise plots of posterior distribution for Sample 1 (yellow is relatively high density, blue is relatively low density). Red lines are best-fit linear trends.

Figure 10 is a "horsetail plot" of model predictions (black lines), for parameter sets sampled randomly from the posterior distribution (after burn-in), compared against the calibration observations (red dots). The mass imbibed model predictions are made out to longer time than the observations (mass imbibed data extend to 10^4 seconds; Figure 6), to illustrate the eventual deviation of the models once they extend beyond the data. The left two panels show the same mass imbibed data plotted on a linear or log time axis. The right panel shows the wetting front position data and model predictions. The model fits the data well.

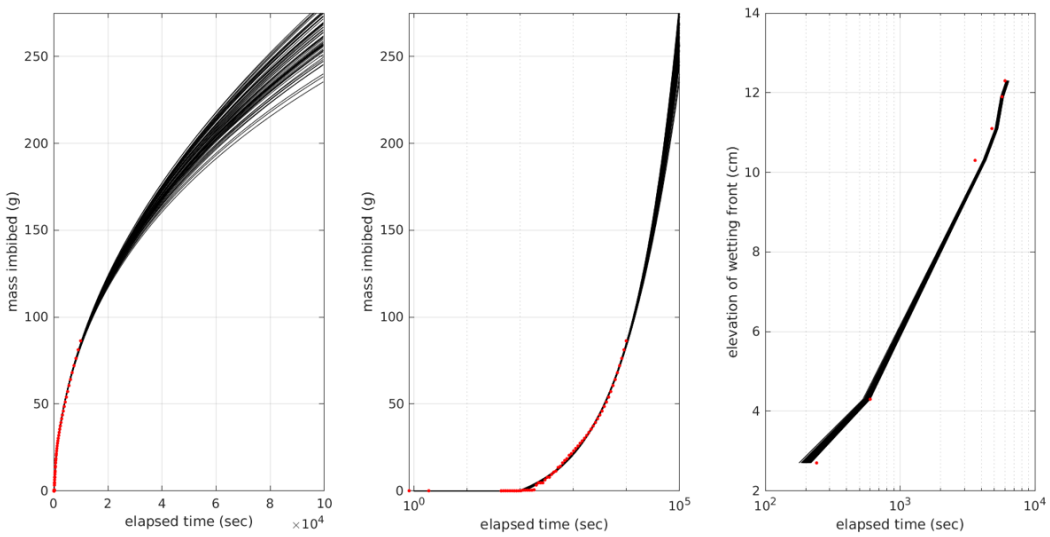

Figure 10. Horsetail plot of 60 models from posterior (black lines) against observations (red dots) for Sample 1. Mass imbibed data are from Figure 6, wetting front data from Table 2.

Figure 11 shows a horsetail plot of the capillary pressure and relative permeability curves, for the same random sample of 60 models from the posterior in Figure 10. The left panel shows the moisture retention curves, the middle plot shows the capacitance function (i.e., the derivative of the curve in the left panel), and the right curve shows the relative permeability curve. To illustrate the effects of porosity and permeability in these figures, the saturation x-axis (left and right panel) is multiplied by porosity to result in a volumetric water content, and the relative permeability y-axis (right panel) is multiplied by intrinsic permeability.

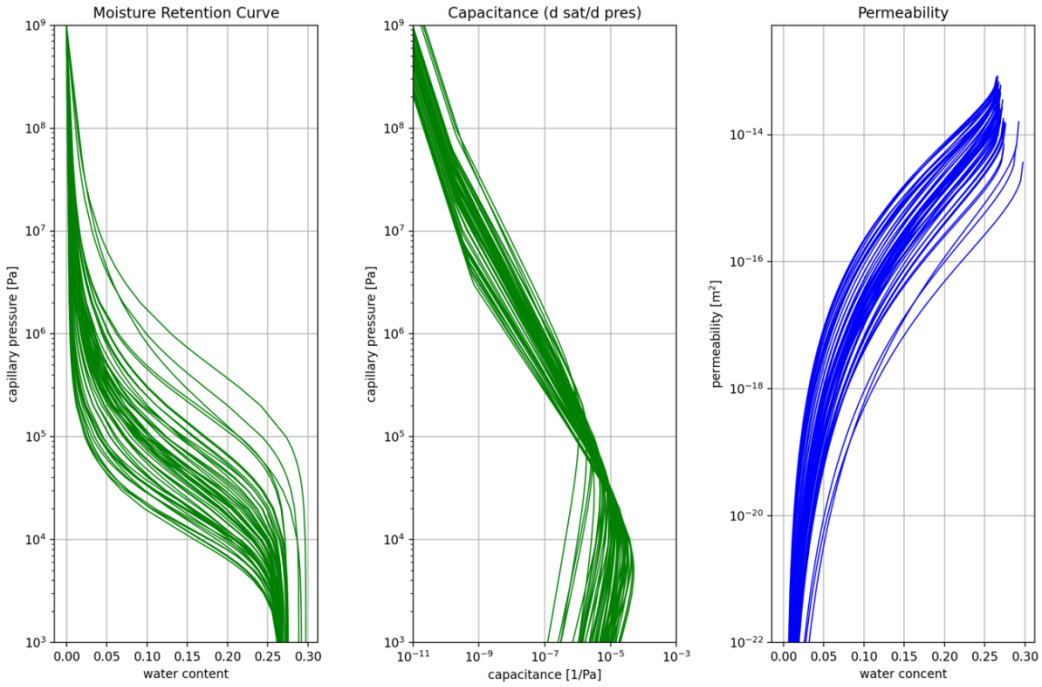

Figure 11. Horsetail plot of 60 moisture retention, capacitance, and relative permeability curves for Sample 1.

Further parameter estimation is performed on the data from this sample in Section 4. This includes a localized sensitivity analysis, predictions of parameters when fitting only subsets of the data, and comparison of the effects of choosing the Mualem or Burdine relationship between the moisture retention curve and the relative permeability curve.

3.2. Sample 2

Sample 2 is UNESE core sample UE-12p#4 895.5-896.5. As based on thin section observations from samples of the same lithofacies (Figure 12), Sample 2 is a zeolitic nonwelded tuff, composed of phenocrysts of quartz and feldspar, lithic fragments, and unflattened pumice in which the volcanic glass has been partially altered to zeolite (clinoptilolite), all in a matrix of zeolitized ash and shard fragments. Smectite from alteration of volcanic glass and patchy opal also occur in this lithofacies. Fluid flow may be affected by the pervasive zeolite and smectite alteration that can occlude previously connected pore space (Figure 12). Core-scale texture includes visible but largely disconnected pore space created by partial dissolution and then zeolite crystallization at the boundaries and within pumice clasts (black regions in the XRCT imaging of Figure 13) within the background, light gray matrix of the zeolitized ash, shard fragments, and smectite, with isolated phenocrysts and lithic fragments hosted in the matrix. No pervasive fracturing at scale of the XRCT imaging is visible.

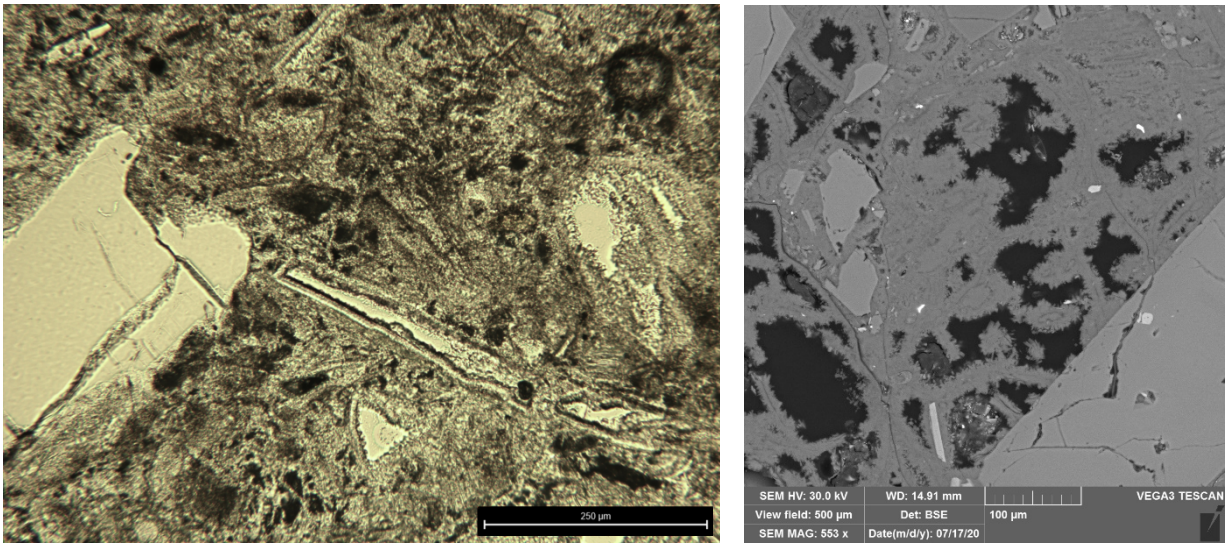

Figure 12. Petrographic image (left) and SEM image (right) showing microtexture of zeolitic nonwelded tuff representative of Sample 2. Tuff consists of quartz and feldspar phenocrysts and volcanic glass that has been altered to zeolite (clinoptilolite) and smectite, partially occluding previously connected pore space.

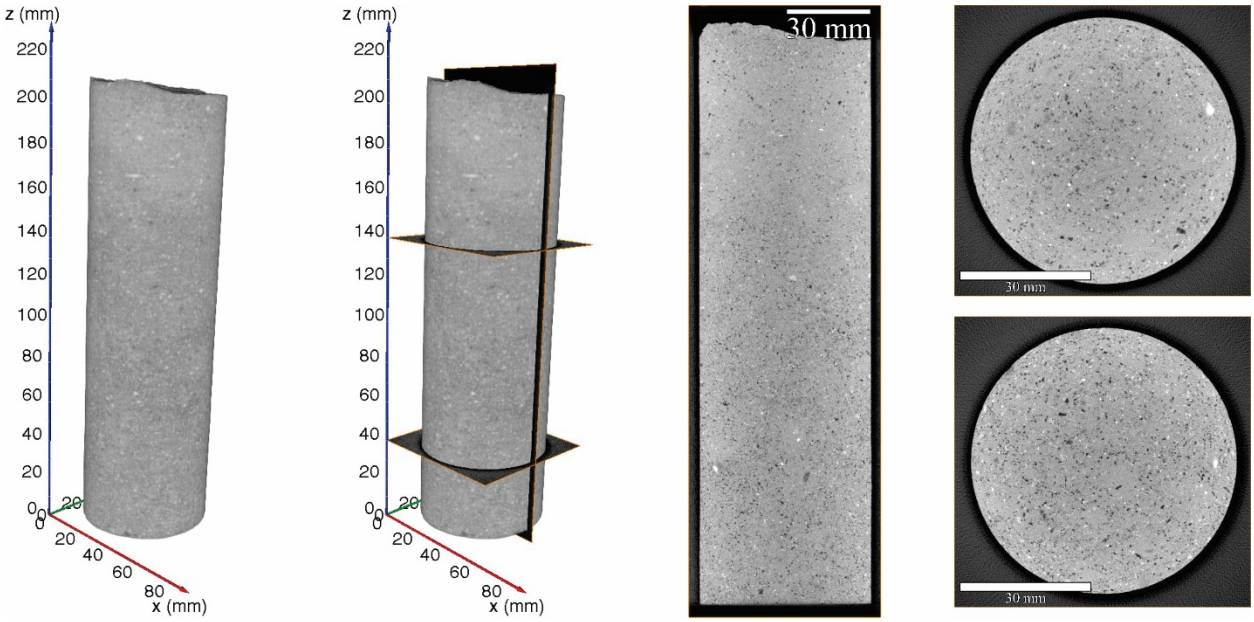

Figure 13. X-Ray CT image montage for Sample 2. Voxel resolution of the XRCT data set is 34.9 µm, with resolvable feature size of approximately 105 µm. 3D rendering on left shows positions of cross-sections on the right, with the upper horizontal plane corresponding to the image on the upper right. Fine-grained texture of phenocrysts, lithic fragments (white), zeolitized matrix volcanic glass (regions of light grayscale values), and largely disconnected pores created by partial zeolitization of pumice (black) are visible in both the 3D renderings and cross-sections.

3.2.1. Laboratory Data

The response of Sample 2 was very different than the other samples, and the imbibition process was much slower. The test on Sample 2 is the only one that ran multiple days (~120 hours), and in that time the wetting front progressed a shorter distance than in the other three samples. Figure 14 shows the mass imbibed data also had significant deviations from the $\sqrt{t}$ behavior typical of imbibition tests (Schmid et al., 2016).

Wetting front observations taken from still images (Table 4) show how slowly the wetting front advanced in this sample (2.44×10^{-8} m/s), approximately 1,000 times slower than the other samples. The photographs in Figure 15 show the slow progress of the wetting front in the sample. After 30 minutes, the initial rise in the water level due to displacement by the sample had still not dissipated.

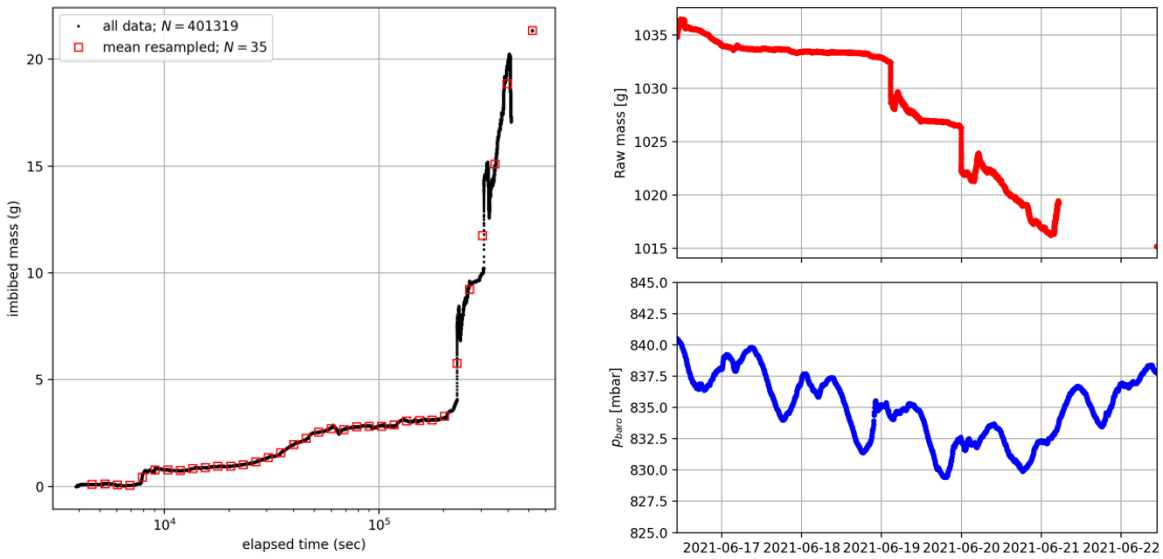

Figure 14. Left: Observed (black dots) and resampled (red squares) data from Sample 2. Right: raw mass data (red) and barometric pressure data measured in the same laboratory (blue).

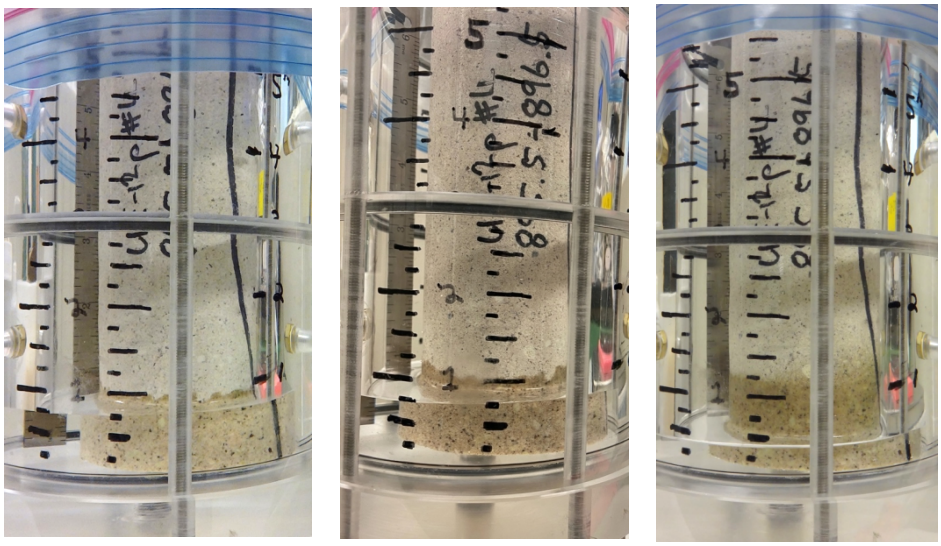

4 minutes 30 minutes 99 hours 30 minutes

Figure 15. Images of the wetting front moving through Sample 2 over time. Numbers on sample holder indicate inches from bottom.

Table 4. Wetting front observations for Sample 2.

Observation Time [hr:min:sec]	Elapsed Time [sec]	Wetting Front Height [m]
2:19:00	8,340	0.0254
26:15:00	94,500	0.028575
99:29:00	358,140	0.03175

3.2.2. *Model Fit to Data*

The MCMC parameter estimation process was not successful in finding an optimal model/data fit for Sample 2 due to two contributing factors. First, the data do not follow the typical shape expected for this type of experiment, indicating it deviates somehow from the conceptual model that is embodied in the PFLOTRAN model. Secondly, the length of the test made each simulation take longer to complete, which makes the overall MCMC process infeasible, since it requires tens of thousands of model evaluations. Figure 16 shows the incomplete results associated with this sample, and Figure 17 shows how the observed data do not fit any of the predicted model shapes.

The sample may have additional processes going on in it, which are not included in the PFLOTRAN model (e.g., swelling, or other moisture-dependent changes happening to the core as it imbibes water; zeolite and smectite may have sorption interactions with the imbibed water, and perhaps wettability differences of certain minerals may have an effect), or the sample may have extreme heterogeneity, which cannot be captured by a single material. Some of the irregularities in the data may be associated with the pressure of the head space in the Mariotte bottle and changes in barometric pressure during the extended test (Figure 14). Typically, the head space prevents water from flowing back into the Mariotte bottle, but fluctuations in barometric pressure may sometimes allow water to flow back, as was observed several times, at approximately 24-hour intervals. Other tests were short enough that barometric pressures did not fluctuate significantly during the test.

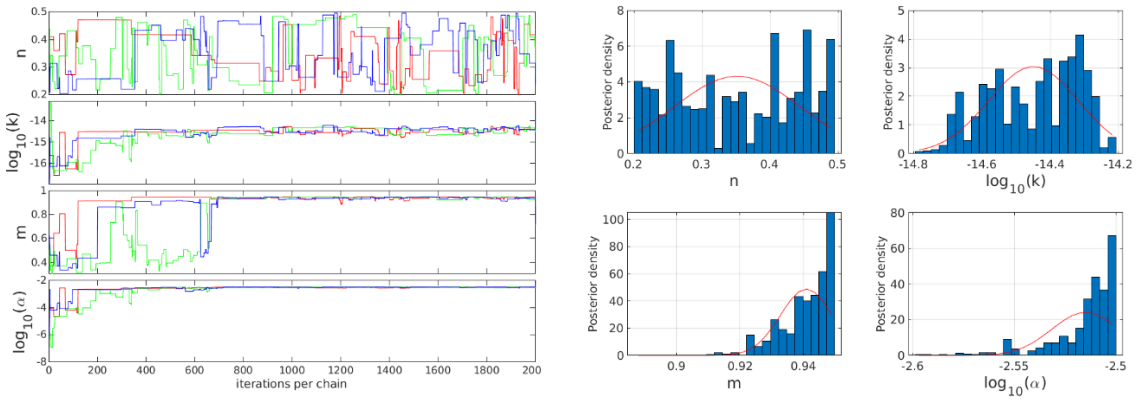

Figure 16. Convergence plot (left) showing evolution of chains and posterior distributions for Sample 2.

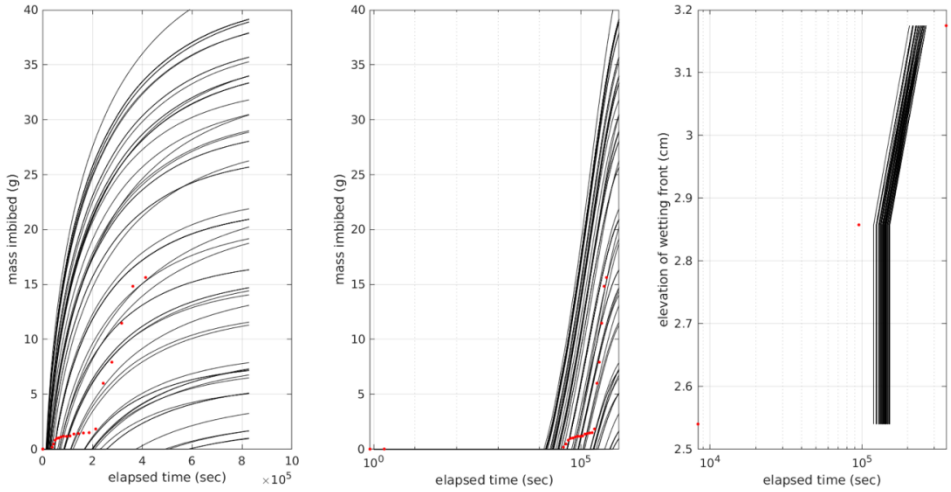

Figure 17. Horsetail plot of 60 models from posterior (black lines) against observations (red dots) for Sample 2 showing the poor fit between model and data.

3.3. Sample 3

Sample 3 is UNESE core sample UE-12p#7 56.2-57.0. As based on thin section observations of other samples in the same lithofacies, Sample 3 is a vitric nonwelded tuff with unflattened glassy pumice, phenocrysts of quartz and feldspar, and lithic fragments in a matrix of fine ash and shard fragments (Figure 18). Core-scale texture (Figure 19) reveals the connected host matrix of volcanic ash, with embedded components having larger sizes than the pumice and phenocrysts of Sample 1.

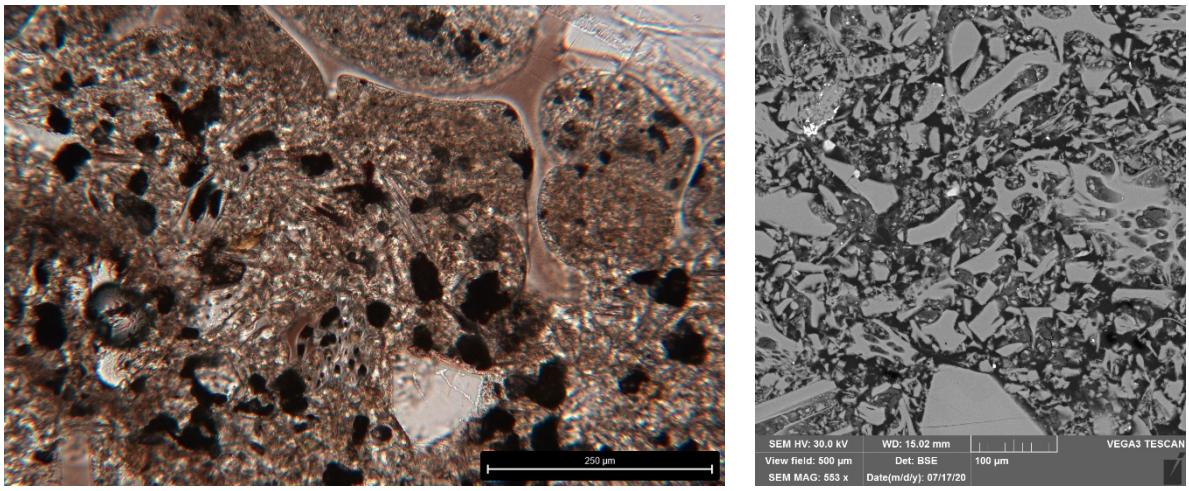

Figure 18. Petrographic image (left) and SEM image (right) showing microtexture of vitric nonwelded tuff representative of Sample 3. Tuff is composed of phenocrysts, lithic fragments, and pumice clasts with partially preserved vesicles that are largely filled with and surrounded by a matrix of fine-grained volcanic ash.

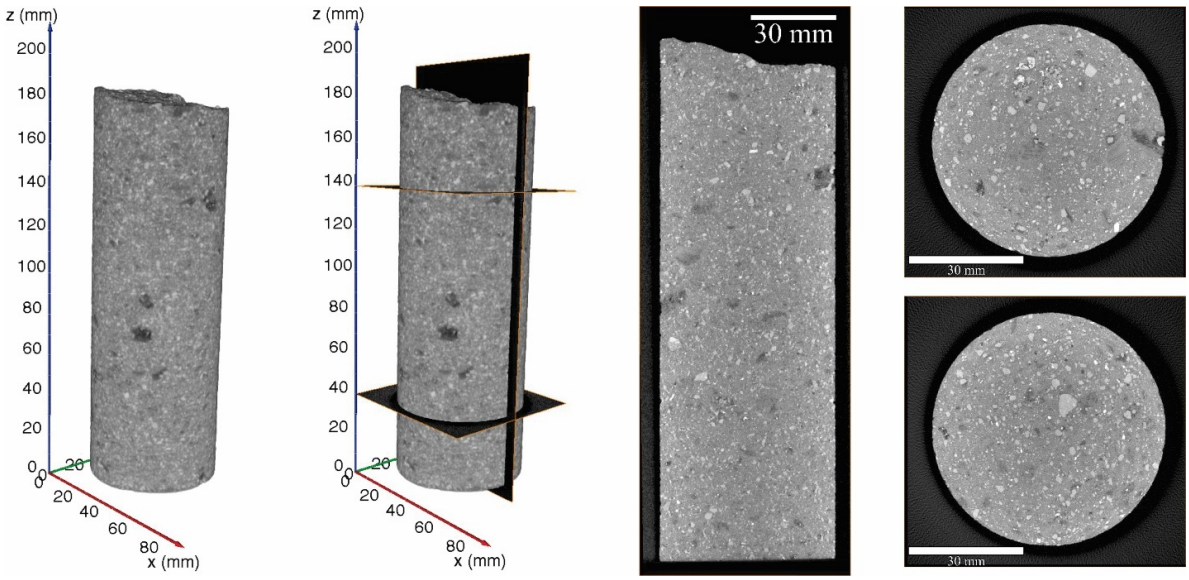

Figure 19. X-Ray CT image montage for Sample 3. Voxel resolution of the XRCT data set is 36.4 µm, with resolvable feature size of approximately 109 µm. 3D rendering on left shows positions of cross-sections on the right, with the upper horizontal plane corresponding to the image on the upper right. Visible sample components include pumice clasts (larger, dark gray to black grains), lithic fragments (brightest grains), phenocrysts, and matrix of volcanic ash. Grain sizes are more variable in this sample compared to Sample 1, which is also a vitric nonwelded tuff.

The XRCT imaging of Sample 3 has variation in grayscale in the radial direction of the core as shown by global grayscale thresholding to the darker pumice clasts near the left and right sides of the vertical cross section through the sample (Figure 20, leftmost image). Correction for this "beam hardening" artifact allows for marker-based watershed segmentation (Figure 20, second, third, and fourth images). The darkest phase of the segmentation (Figure 20, rightmost image) may represent pumice clasts (volume fraction of 0.034), including associated relatively large vesicles seen in thin sections (Figure 18). The next lighter phase in the segmentation is the matrix of volcanic ash (volume fraction of 0.860). The last two relatively bright phases are phenocrysts and lithic fragments (volume fractions of 0.102 and 0.004, respectively). Larger pumice clasts are distributed throughout the sample and generally do not touch (Figure 21)— more sophisticated machine-learning based segmentation and size/shape quantification for this complex sample is left for future work.

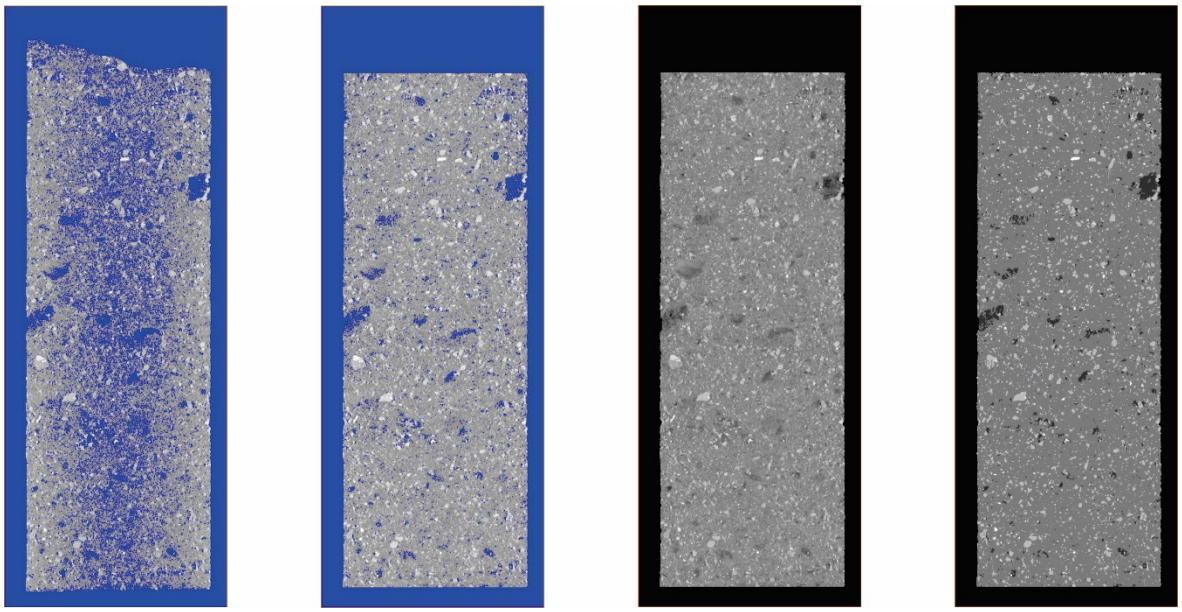

Figure 20. Examples of image post-processing as shown for the XRCT vertical cross of Figure 19 for Sample 3. Global thresholding on uncorrected and corrected images (leftmost two images). The cross-section after edge-preserving bilateral filtering (third image from left). Segmentation for four phases using the marker-based watershed method (image on the far right). The second, third, and fourth images from the left are rendered at the same size as the image on the left (and as the same image in Figure 19) but cropped to remove irregularities at the top and bottom of the sample.

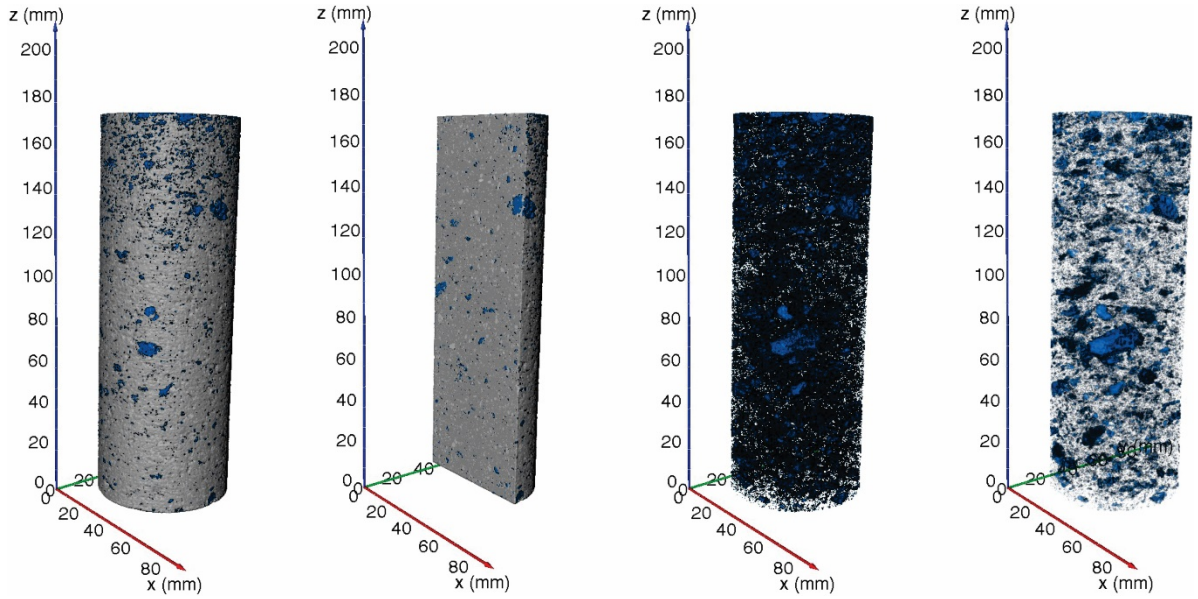

Figure 21. Various 3D renderings of the segmented data set (especially the darkest segmented phase of the rightmost image of Figure 20). Segmentation rendered with the darkest phase in blue, with the other phases in grayscale like the rightmost image of Figure 20 (far left). Rendering cut in half at the location of the cross section of Figure 19 (second from the left). Rendering of only the darkest phase in blue (third from left). Rendering of the darkest phase, but with the transparency factor adjusted to allow better visualization of the relatively larger pumice clasts (far right).

3.3.1. Laboratory Data

The mass imbibed data have a gap (Figure 22) because an issue occurred with the Python script used to collect data from the balance. An unhanded communication error came from the PyVISA library. The script was then modified to handle exceptions. Wetting front observations (Table 5) were taken from video. The wetting front speed is computed to be 1.41×10^{-5} m/s from these observations. Figure 23 shows images of the wetting front progress during the experiment.

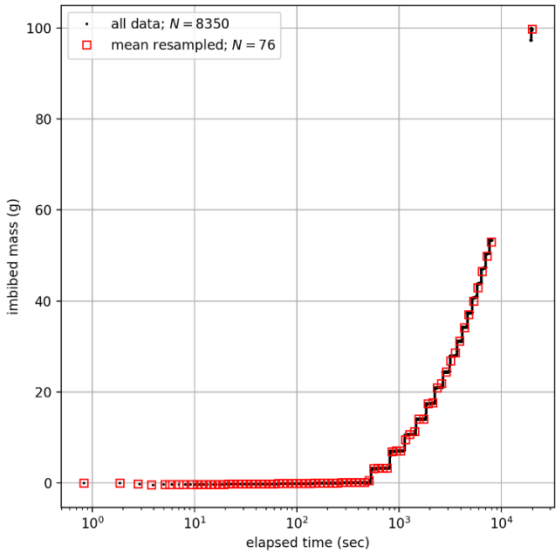

Figure 22. Observed (black dots) and resampled (red squares) data from Sample 3.

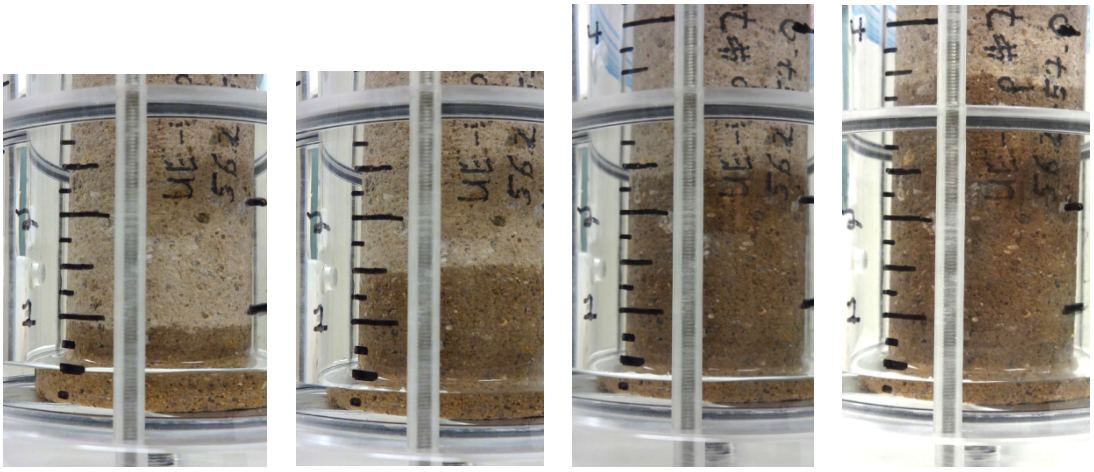

2 minutes 20 minutes 60 minutes 120 minutes

Figure 23. Images of the wetting front moving through Sample 3 over time. Numbers on sample holder indicate inches from bottom.

Table 5. Wetting front observations for Sample 3.

Observation Time [min:sec]	Elapsed Time [sec]	Wetting Front Height [m]
0:29	0	0
4:14	225	0.0254
11:33	664	0.03175
19:14	1,125	0.0381
23:24	1,375	0.041275

3.3.2. Model Fit to Data

The convergence of the MCMC model is illustrated in the left panel Figure 24, where the burn-in period is less than 2000 iterations per chain, while 40,050 total iterations were completed (13,350 iterations per chain). The chains (excluding the burn-in period) are plotted as histograms in the right panel of Figure 24 with red cuves showing bets-fit Gaussian curves with the same mean and variance as the distribution (summarized Table 6). The two log-transformed parameters (k and α) both have similar highly skewed distributions.

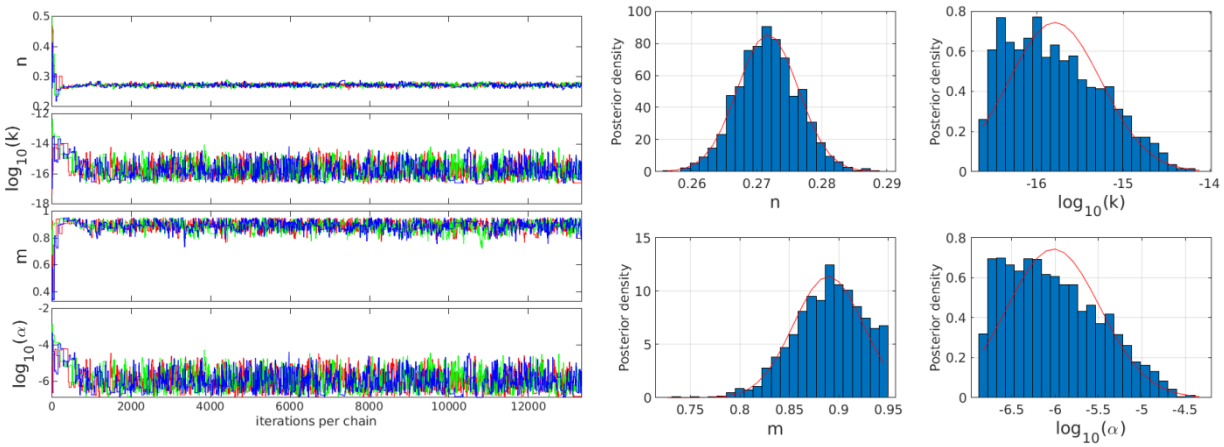

Figure 24. Left: convergence plot showing evolution of chains for Sample 3. Right: histograms of posterior with best-fit Gaussians in red.

Table 6. Statistics on posterior distribution for Sample 3.

Parameter [units]	Mean	Variance	Mode
Porosity (n) [-]	0.272	2.17×10^{-5}	0.271
Permeability (k) [m^2]	$10^{-15.79}$	2.87×10^{-1}	$10^{-16.00}$
van Genuchten m [-]	0.889	1.23×10^{-3}	0.891
van Genuchten α [1/Pa]	$10^{-6.02}$	2.88×10^{-1}	$10^{-6.62}$

Relating the air-entry pressure (α ranging approximately from 10^{-5} to 2.5×10^{-7} in Figure 24) to a pore radius size using equation (10) results in a range of characteristic pore radius size from 1.4 to 0.04 μm, which would be too small to resolve on the microscopic images of Figure 18.

Figure 25 shows the pairwise distributions of the posterior, illustrating the strong positive correlation between k and α, and the generally weak correlations between the other parameters.

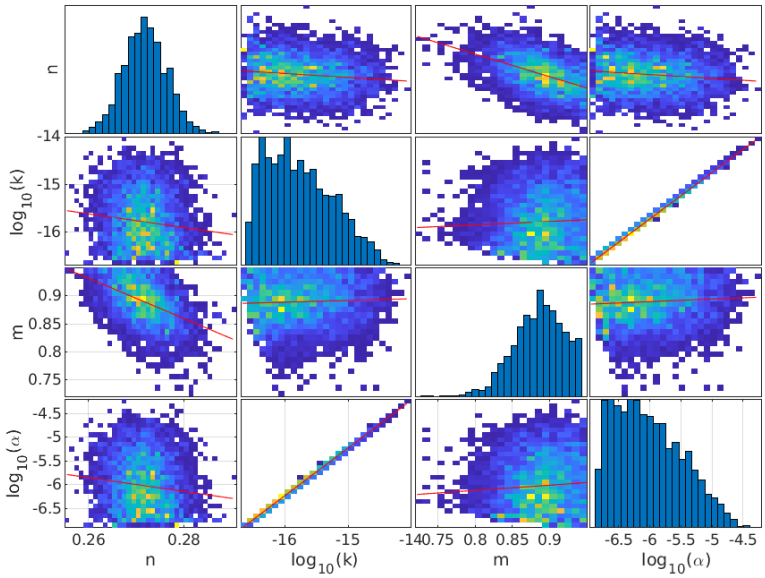

Figure 25. Pairwise plots of posterior distribution for Sample 3 (yellow is relatively high density, blue is relatively low density). Red lines are best-fit linear trends.

Figure 26 shows the horsetail plots of the model/data fit. The model prediction is made out three times further than the last mass imbibed data (20,000 seconds; Figure 22) Like Sample 1, the fit of the model to the data is generally good, but one early wetting front observation at 2.54 cm and 225 seconds is missed significantly by the model.

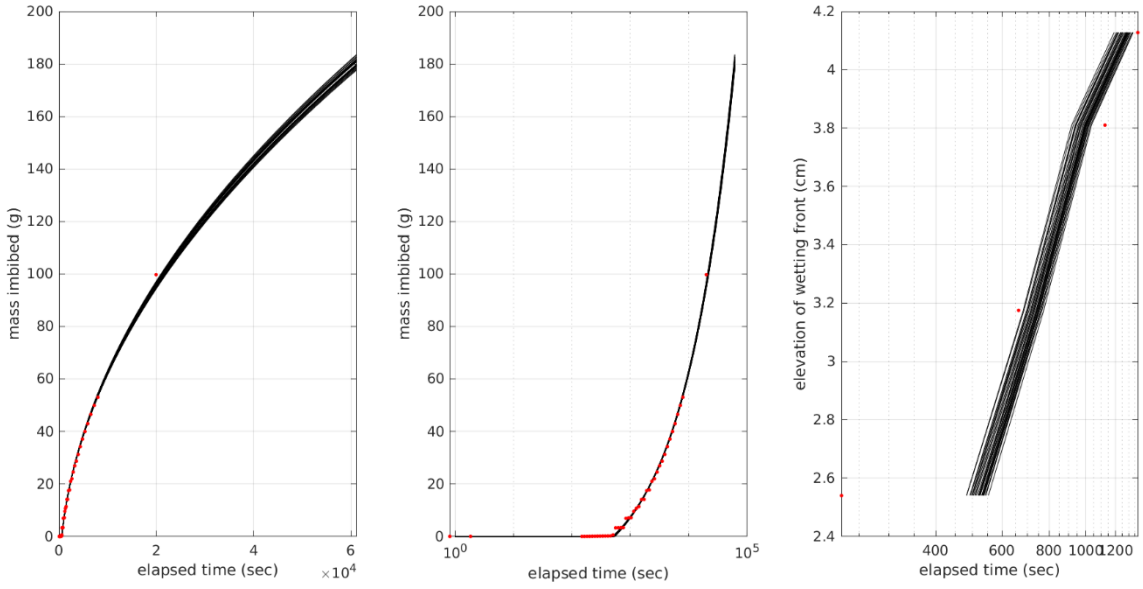

Figure 26. Horsetail plot of 60 models from posterior (black lines) against observations (red dots) for Sample 3. Mass imbibed data are from Figure 22, wetting front data from Table 5.

Figure 27 shows the moisture retention curve, the capacitance, and the relative permeability curves associated with the same samples drawn randomly from the posterior distribution shown in Figure 26. The relatively wide range of α from the parameter estimation manifests in relative uncertainty in

the vertical position of the capillary pressure curves in the left panel of Figure 27. The relative uncertainty in the permeability results in a wide band of permeability curves in the right panel of Figure 27.

The capacitance curve (middle panel Figure 27) is the derivative of the moisture retention curve and illustrates the benefit of the loop_invariant and unsaturated_extension additions to PFLOTRAN. This type of capillary pressure curve (relatively high value of m, near 1), would previously be associated with numerical issues in PFLOTRAN because the derivative of moisture retention curve would be zero for a wide range of capillary pressures. The exponential unsaturated extension produces the linear slope on a log-log plot in the middle panel at higher capillary pressures.

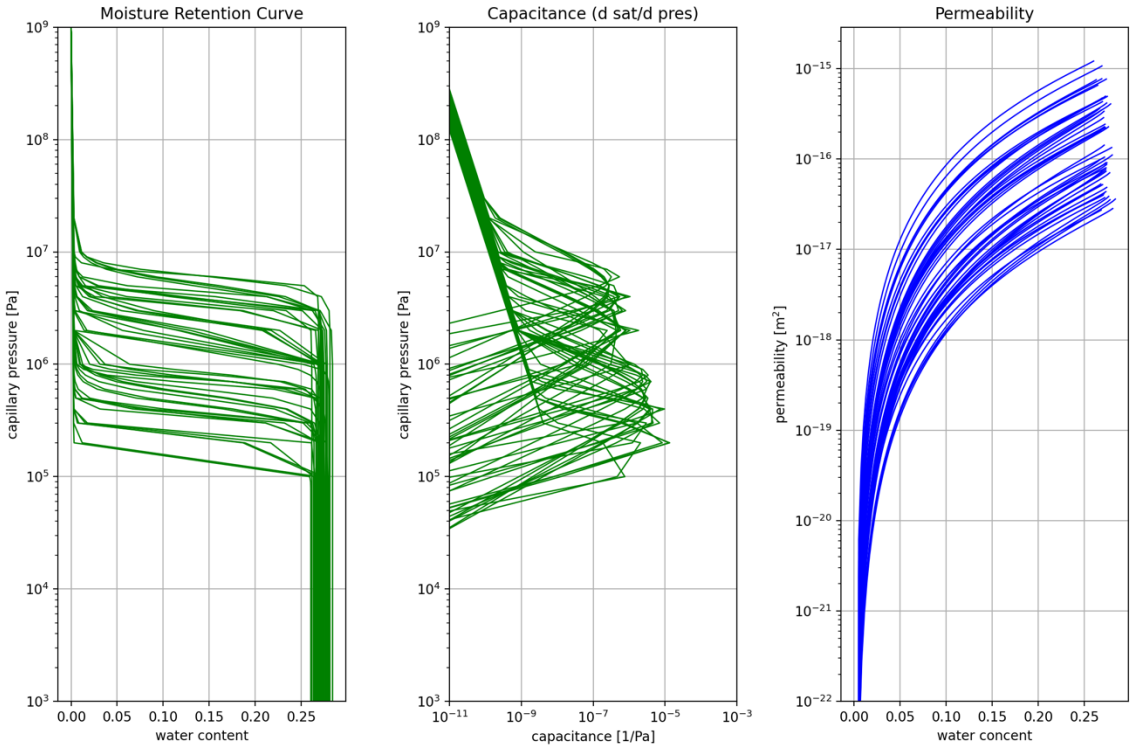

Figure 27. Horsetail of 60 moisture retention, capacitance, and relative permeability curves for Sample 3.

3.4. Sample 4

Sample 4 is UNESE core sample UE12p#4 32.2-32.9. As based on thin section observations from samples in the same lithofacies (Figure 28), Sample 4 is a vitric nonwelded tuff with phenocrysts of quartz and feldspar, lithic fragments, and unflattened, glassy pumice with preserved pumice vesicles in a matrix of ash and glass shards. Texture at the core scale includes large and highly porous pumice clasts, with other smaller lithic clasts and phenocrysts, hosted in the fine-grained ashy matrix. The ashy matrix appears to still be the predominate connected phase in the vertical direction.

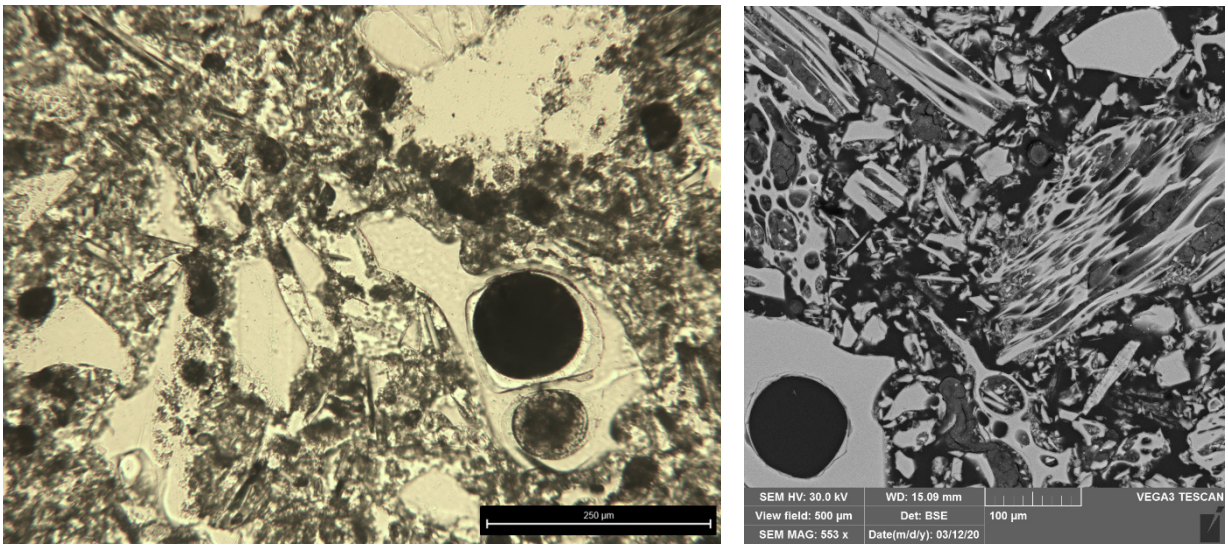

Figure 28. Petrographic image (left) and SEM image (right) showing microtexture of vitric nonwelded tuff representative of Sample 4 with phenocrysts, lithic fragments, and pumice clasts that commonly contain preserved pumice vesicles, all in a loose matrix of volcanic ash.

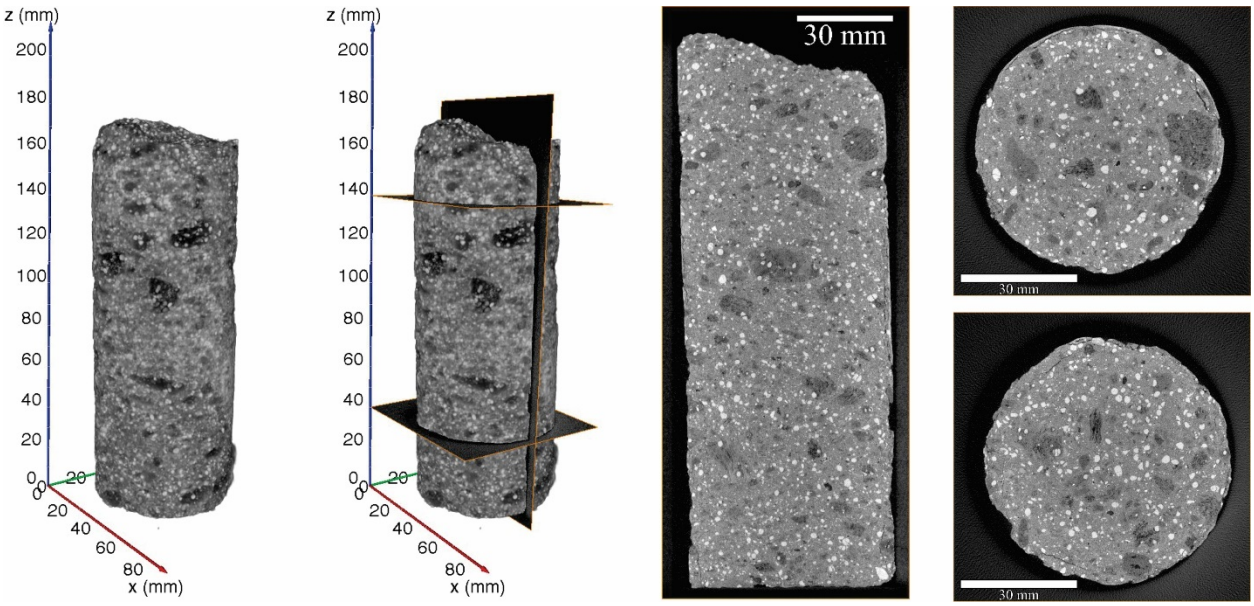

Figure 29. X-Ray CT image montage for Sample 4. Voxel resolution of the XRCT data set is 37.5 µm, with resolvable feature size of approximately 113 µm. 3D rendering on left shows positions of cross-sections on the right, with the upper horizontal plane corresponding to the image on the upper right. Large, highly porous pumice clasts (dark gray) are visible in both the reconstruction and cross-sections. Smaller, brighter lithic clasts and phenocrysts, as well as fine-grained, ashy matrix surrounding all grains are also visible.

3.4.1. Laboratory Data

Observed mass imbibed is plotted in Figure 30, and the observations of the wetting front elevation (taken from video) used for model calibration elevation are listed in Table 7. The wetting front speed was estimated as 6.12×10^{-5} m/s from these observations. Figure 31 shows images of the wetting front migration during the experiment.

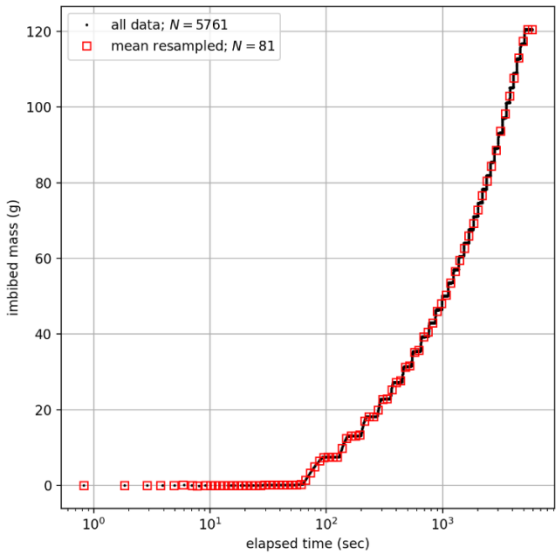

Figure 30. Observed (black dots) and resampled (red squares) data from Sample 4.

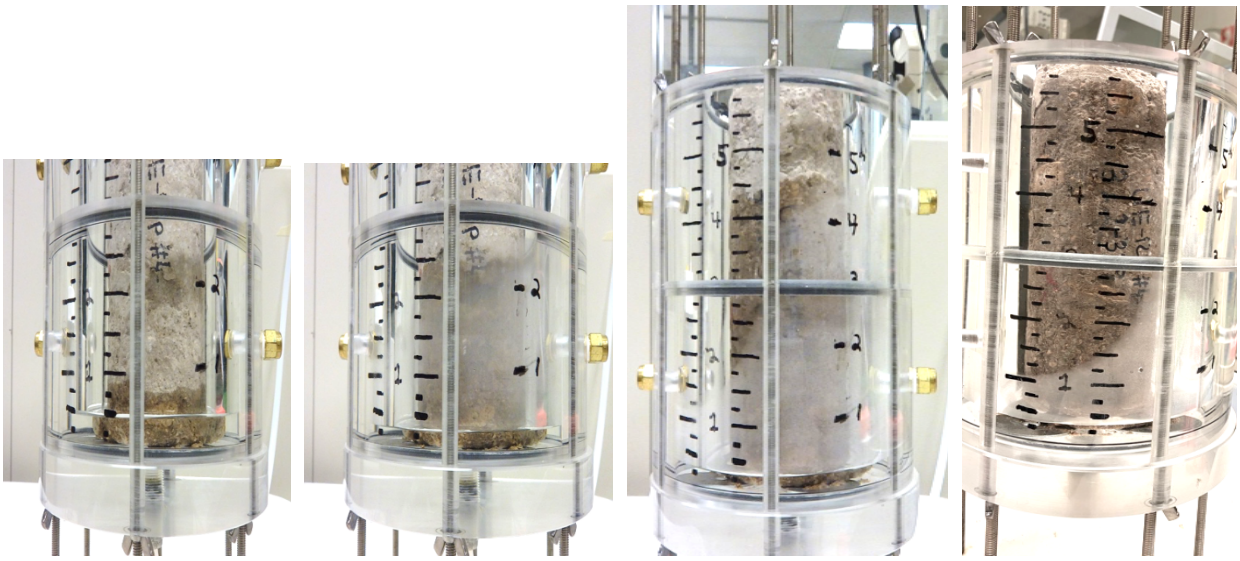

Figure 31. Images of the wetting front moving through Sample 4 over time. Numbers on sample holder indicate inches from bottom.

Table 7. Wetting front observations for Sample 4.

Observation Time [min:sec]	Elapsed Time [sec]	Wetting Front Height [m]
1:21	0	0
2:45	84	0.03175
3:53	152	0.0381
7:00	339	0.0508
10:12	531	0.0635
16:00	879	0.0762
21:00	1,179	0.0889

3.4.2. Model Fit to Data

The entire MCMC results are shown in the left panel of Figure 32. The burn-in period is the first 2,000 iterations per chain, while a total of 40,050 iterations total were used (13,350 iterations per chain).

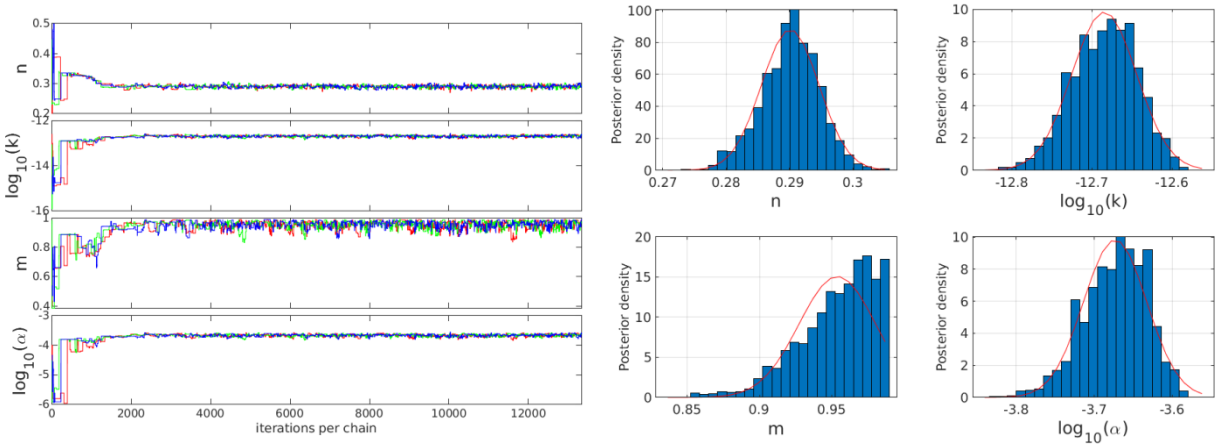

Figure 32. Left: convergence plot showing evolution of chains for Sample 4; right: histograms of posterior, showing best-fit Gaussians (red).

The chains (less the first 2,000 iterations during burn-in) are plotted as histograms in Figure 32. Red curves illustrate Gaussian distributions with the same mean and variance as the posterior; posterior statistics are listed in Table 8.

Figure 33 shows the pairwise distributions of the posteriors, indicating strong positive correlation between α, m, and k, and little correlation between porosity and the other parameters.

Table 8. Statistics on posterior distribution for Sample 4.

Parameter [units]	Mean	Variance	Mode
Porosity (n) [-]	0.290	2.06×10^{-5}	0.291
Permeability (k) [m^2]	$10^{-12.69}$	1.65×10^{-3}	$10^{-12.68}$
van Genuchten m [-]	0.954	7.03×10^{-4}	0.974
van Genuchten α [1/Pa]	$10^{-3.67}$	1.65×10^{-3}	$10^{-3.67}$

Relating the air-entry pressure (α=2.1×10^{-4} [1/Pa]) to a pore radius size using equation (10) results in a range of characteristic pore radius size of 30 μm, which is of the same order of magnitude as that observed in the microscope images of Figure 28.

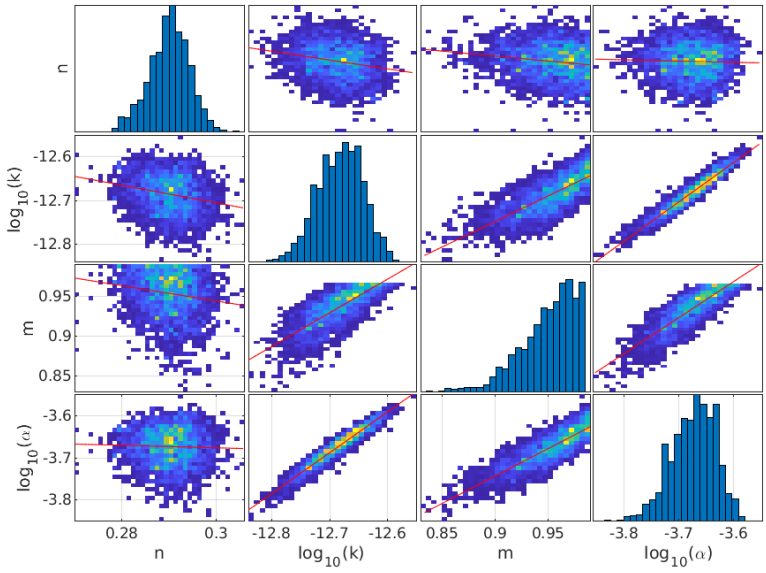

Figure 33. Pairwise plots of posterior distribution for Sample 4 (yellow is relatively high density, blue is relatively low density). Red lines are best-fit linear trends.

Figure 34 shows the horsetail plot of model/data fit, which is also in general good, but there is some deviation between early-time wetting front elevations and model predictions. The model prediction goes 10 times further than the last mass imbibed data (~6,000 seconds; Figure 30). Figure 35 shows the horsetail plot of the moisture retention curve, capacitance, and relative permeability for the same 60 random samples from the posterior. Compared with Sample 3, Sample 4 has a relatively narrow estimate of both m and α, which results in a very narrow cluster of all three curves.

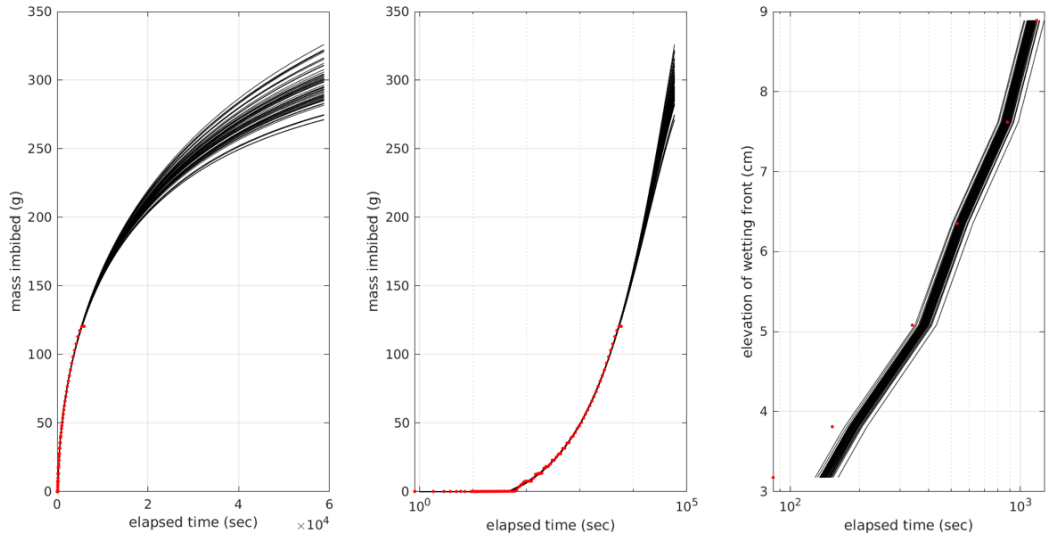

Figure 34. Horsetail plot of 60 models from posterior (black lines) against observations (red dots) for Sample 4. Mass imbibed data are from Figure 30, wetting front data from Table 7.

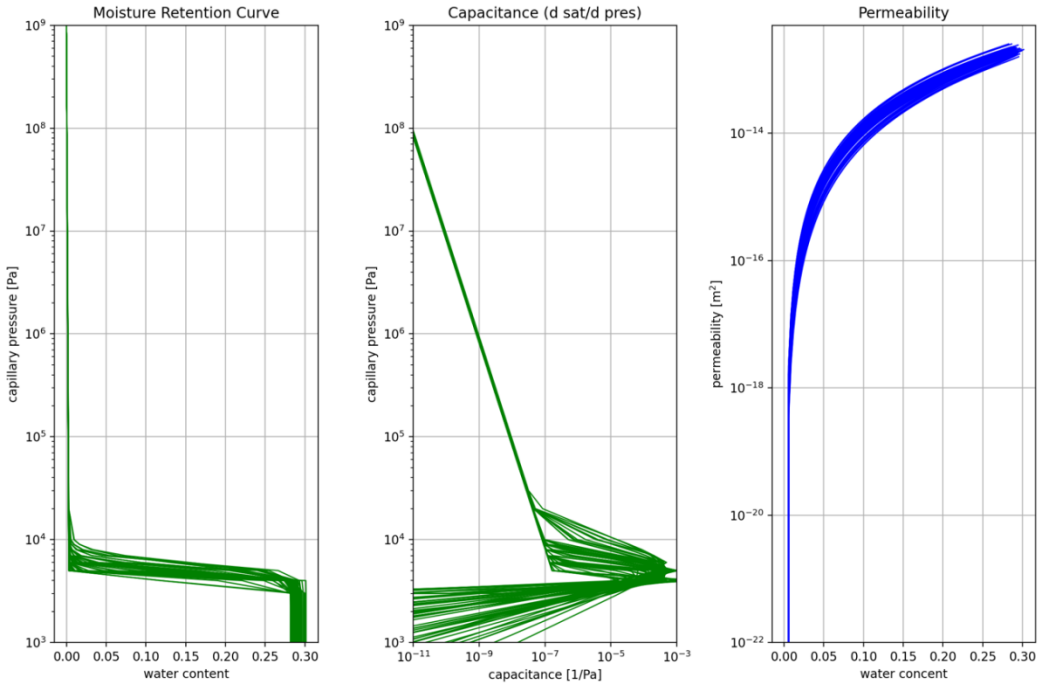

Figure 35. Horsetail of 60 moisture retention, capacitance, and relative permeability curves for Sample 4.

4. PARAMETER SENSITIVITY AND DATA IMPORTANCE

Additional simulations were conducted to confirm and explore the parameter estimation process using data collected from Sample 1. These simulations were done to investigate the role different data types have in the parameter estimation process.

4.1. Sample 1 Parameter Sensitivity

The gradient-based parameter estimation tool PEST (Doherty, 2015) was used to automatically estimate sensitivities of parameters for Sample 1. PEST was run using the same model used in the DREAM analysis, starting with at the optimum (i.e., mode) values listed in Table 3 as the initial guess, using the same parameter ranges.

Table 9. PEST-Estimated Parameters and 95% Confidence Limits for Sample 1.

Parameter	Estimated Value	95% Confidence Limits	
		Lower	Upper
Porosity (n)	0.266	0.262	0.268
Permeability (k)	6.36×10^{-14}	6.07×10^{-14}	6.67×10^{-14}
van Genuchten m	0.432	0.420	0.445
van Genuchten α	9.46×10^{-5}	9.36×10^{-5}	9.57×10^{-5}

The PEST estimated values are close to the peaks of the posterior distribution from the MCMC analysis, but the confidence limits reported by PEST are less informative than the pairwise plots of the posterior distributions.

PEST reduces model-data misfit through explicit calculation of a Jacobian matrix, using finite differences to approximate derivatives. Each free parameter is independently perturbed a small amount, the model is re-run, and the subsequent change in each observation is quantified. The Jacobian matrix can then be plotted to show the scaled sensitivity of each parameter through time. Figure 36 shows the columns of the PEST-computed Jacobian, plotted against the corresponding times associated with each observation. This shows the magnitude of the parameter sensitivity to the change in mass imbibed increases with time, and the all the parameters except van Genuchten α are positively correlated at later time (i.e., positive correlation indicates an increase in a parameter leads to an increase in model/data residual). At early time, all the parameters start off with a smaller negative sensitivity.

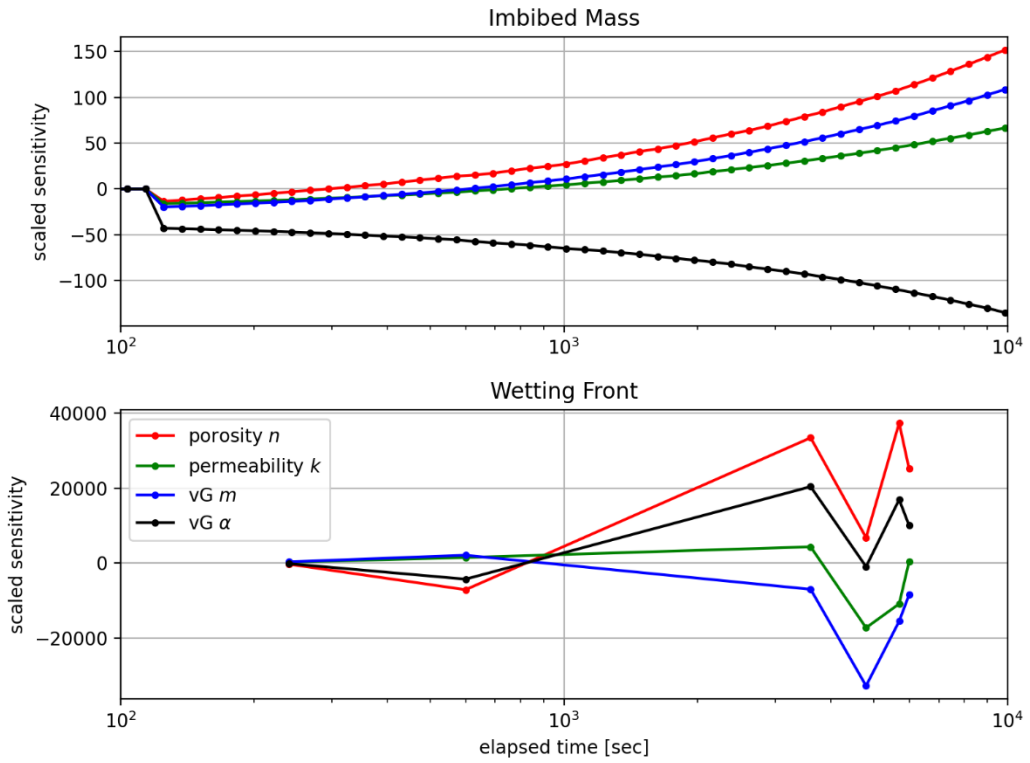

Figure 36. Scaled PEST-computed sensitivity of imbibed mass (top) and wetting front (bottom) data through time for Sample 1.

For wetting front observations, the relative magnitude of the sensitivities is much larger than for the mass imbibed observations, but this is partially due to the difference in units between the two data types (grams of water vs. time in seconds). The sensitivity of the wetting front observations is related to whether the model lags or is ahead of the observed wetting front time (see Figure 10). For the wetting front observation at 400 seconds, the model is behind the observation, while the for the later wetting front observations, the model is ahead of observations (the observation at 4,800 seconds is less behind than the others, and the sensitivity there is less, too).

For the wetting front location data porosity and van Genuchten α have similar trends, and permeability and van Genuchten m also have a similar trend, nearly opposite of the other two.

The sensitivity data shows later-time data are valuable, which also means longer cores are valuable.

4.2. Sample 1 MCMC Results with Mass Imbibed Data Only

Like the process outlined in Section 3.1, the DREAM MCMC parameter estimation process was repeated using only the mass imbibed data, leaving out the wetting front observations. Figure 37 shows the resulting posterior distributions when only using the mass-imbibed data as a calibration target. Although not shown, the burn-in period was less than 1,000 iterations per chain, and 40,050 total iterations were run. Green curves in the posterior histograms illustrate the results when using both datasets (i.e., the red curves from Figure 8). Table 10 summarizes the statistics on the posterior illustrated in the histograms of Figure 37, including the mode when using all data for comparison.

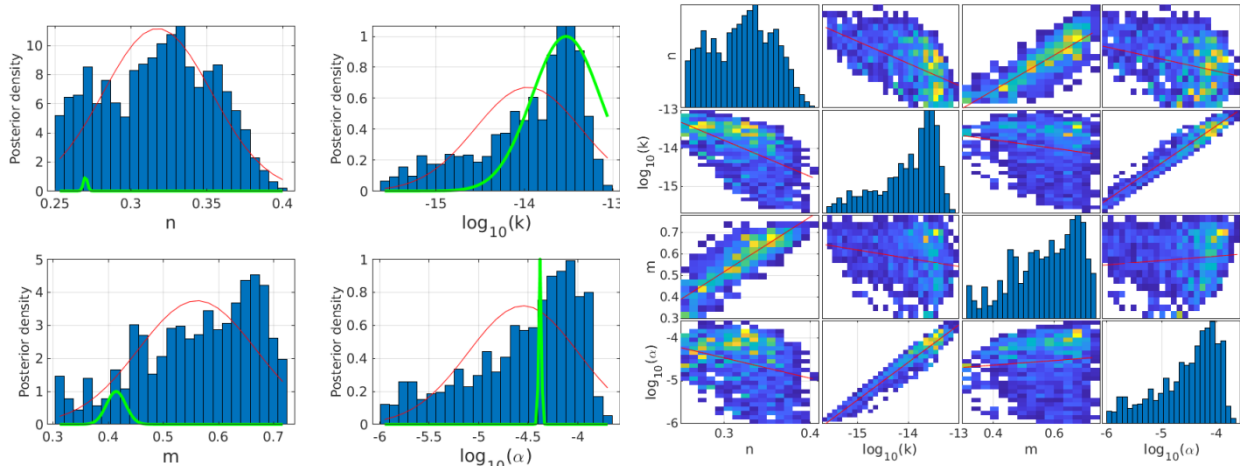

Figure 37. MCMC posterior distribution for Sample 1 using only mass imbibed time series (no wetting front data). left: posterior histograms (green curves are Gaussians from Figure 8); right: pairwise posterior distributions.

The permeability and van Genuchten α have slightly different, but similar estimated values with and without the wetting front data, but the van Genuchten m and porosity values are notably different without the wetting front data.

Table 10. Statistics on posterior distribution for Sample 1, calibrating only to mass imbibed data.

Parameter [units]	Mean	Variance	Mode	Mode w/ all data
Porosity (n) [-]	0.317	1.27×10^{-3}	0.333	0.266
Permeability (k) [m^2]	$10^{-13.96}$	3.53×10^{-1}	$10^{-13.58}$	$10^{-13.21}$
van Genuchten m [-]	0.561	1.13×10^{-2}	0.666	0.398
van Genuchten α [1/Pa]	$10^{-4.55}$	3.08×10^{-1}	$10^{-4.07}$	$10^{-4.00}$

The horsetail plot of the model/data results (Figure 38) shows the constraint of the wetting front observations clearly results in less scatter for the wetting front prediction. Without the wetting front observations, the quality of the fit to the mass imbibed data is similar, but the predictions of wetting front elevation are generally behind those observed.

The horsetail plot (Figure 39) of the capillary pressure curves shows a much larger spread in all the curves, due to the larger uncertainty in porosity and the van Genuchten m parameter (yellow curves

in Figure 39 are the horsetail plot curves from Figure 11). Additional uncertainty in the van Genuchten α parameter results in a wider spread vertically in the moisture retention curves.

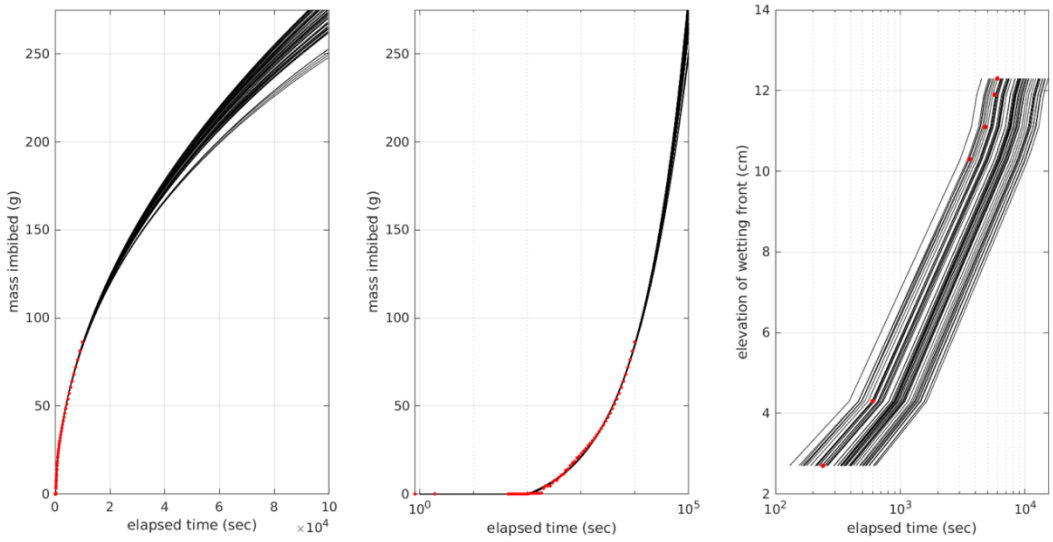

Figure 38. Horsetail plot of 60 models from posterior (black lines) against observations (red dots) for Sample 1, calibrating only to mass imbibed data.

Clearly, the wetting front observations have a large impact on the uniqueness of the best fit parameters. The best estimate of permeability appears to be the least impacted by leaving out the wetting front observations, while both the estimated values and variances of the other three parameters are significantly impacted by leaving out the wetting front data.

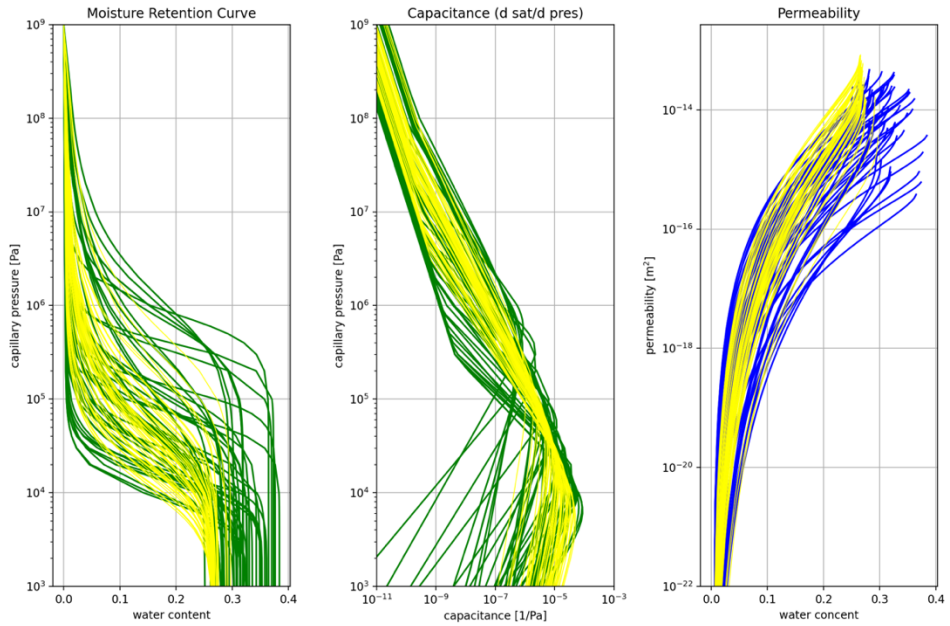

Figure 39. Horsetail of 60 moisture retention, capacitance, and relative permeability curves for Sample 1, calibrating only to mass imbibed data. Yellow curves from Figure 11 include all data.

4.3. Model Fit to Wetting Front Data Only

Complementary to the previous section that left out the wetting front data, this section illustrates the impact of leaving out the mass imbibed data, and only using the six wetting front observations to calibrate the model. Figure 40 shows the histogram and pairwise plots of the posterior distribution. Although not shown here, the burn in period was less than 1,000 iterations per chain, and a total of 40,050 iterations were taken.

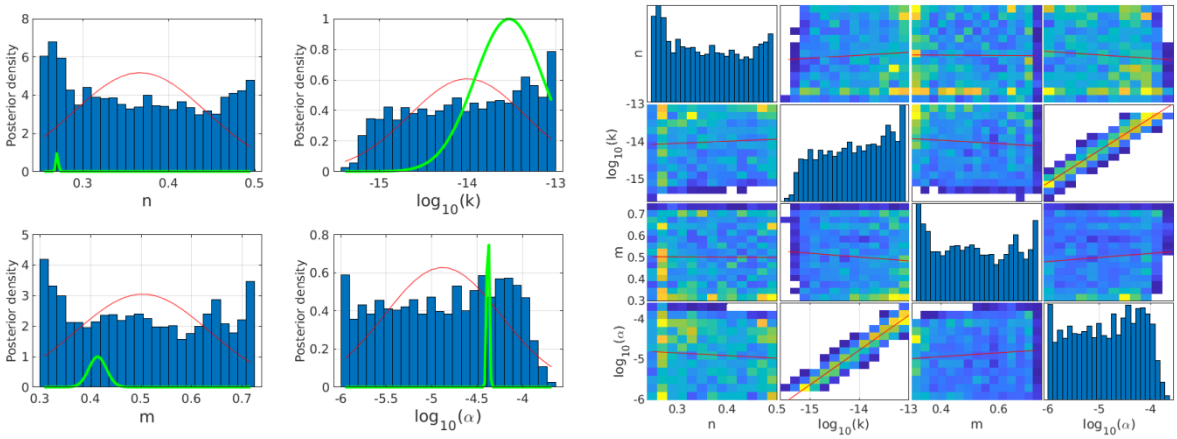

Figure 40. MCMC Posterior distribution for Sample 1 using only wetting front observations (no mass imbibed data). Left: posterior histograms (green curves from Figure 8); right: pairwise posterior plots.

Compared to using only the mass imbibed data, using only the wetting front observations resulted in a much more uncertain fit of the model and data (Table 11)—Figure 40 shows the posteriors cover much of the allowed parameter range. Only the porosity reported a similar value (mode), while all the other parameters had both very different best-estimates and uncertainties. The correlation between k and α is still strong, as seen in the pairwise plots.

Table 11. Statistics on posterior distribution for Sample 1, calibrating only to wetting front data.

Parameter [units]	Mean	Variance	Mode	Mode w/ all data
Porosity (n) [-]	0.366	5.93×10^{-3}	0.265	0.266
Permeability (k) [m^2]	$10^{-14.00}$	4.29×10^{-1}	$10^{-13.05}$	$10^{-13.21}$
van Genuchten m [-]	0.503	1.71×10^{-2}	0.309	0.398
van Genuchten α [1/Pa]	$10^{-4.88}$	4.04×10^{-1}	$10^{-5.95}$	$10^{-4.00}$

The horsetail plot of model results and data (Figure 41) clearly shows the impact of not calibrating to the mass imbibed data. The wetting front elevations are constrained, but most of the mass imbibed model curves predict higher mass imbibed than was observed at any given time.

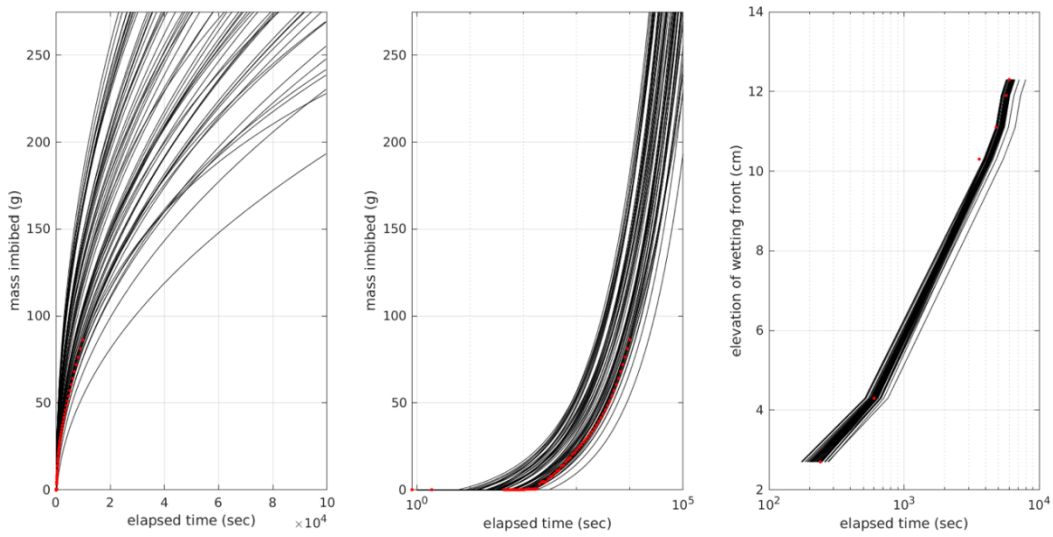

Figure 41. Horsetail plot of 60 models from posterior (black lines) against observations (red dots) for Sample 1, calibrating only to wetting front data.

Despite the much more uncertain parameters, the spread shown in the capillary pressure horsetail plots (Figure 42) is not much different from Section 4.2, with the wetting front data left out. The parameter estimates are less constrained, but they both are limited by the same upper and lower parameter bounds imposed on the entire parameter estimation process.

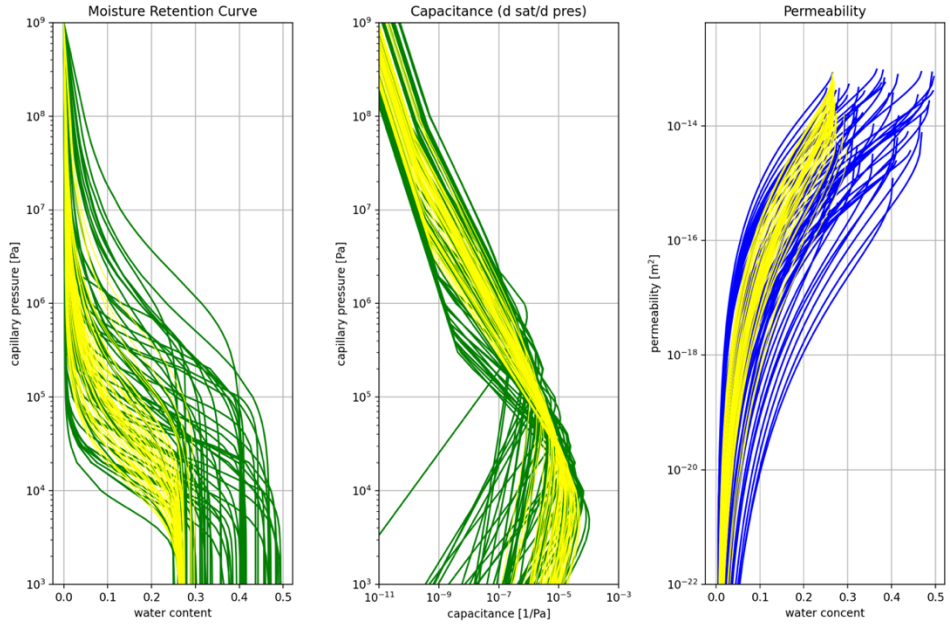

Figure 42. Horsetail of 60 moisture retention, capacitance, and relative permeability curves for Sample 1, calibrating only to wetting front data. Yellow curves from Figure 11 include all data.

4.4. Comparison of Burdine and Mualem Relative Permeability Models

To illustrate the sensitivity of the method to parametric form of the moisture retention curve and the relative permeability curve, we re-fit the Sample 1 data using the van Genuchten/Burdine relative permeability model (Equation 9). If the parameter estimation approach were only sensitive to the capillary pressure curve (i.e., the relative permeability curve was simply being predicted), the fit should be the same for the two models, since in the PFLOTRAN implementation they share the same moisture retention curve.

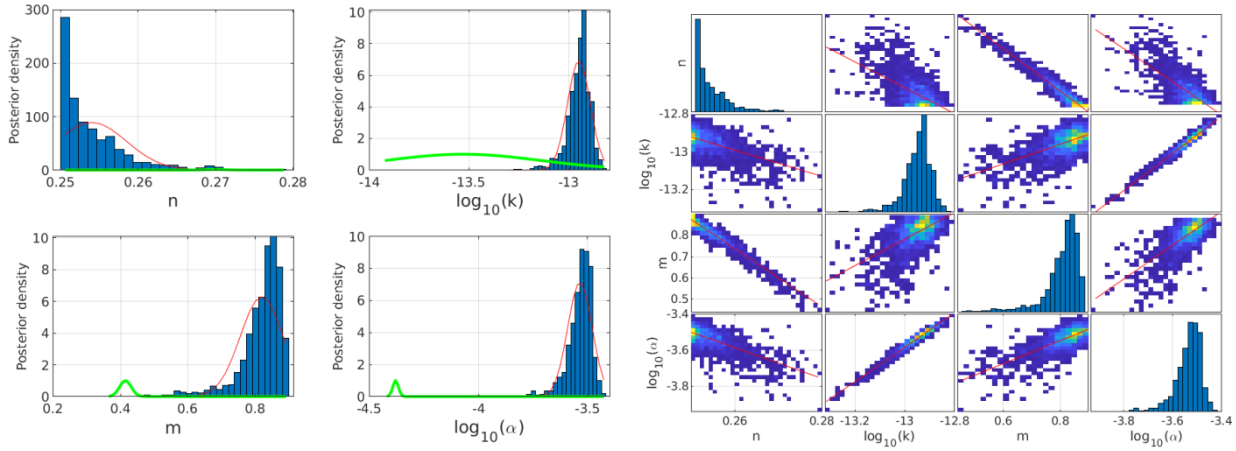

Figure 43. MCMC Posterior distribution for Sample 1 using Burdine relative permeability. Left: posterior histograms (green curves from Mualem in Figure 8); right: pairwise posterior plots.

Figure 43 shows the posterior distribution from re-calibration. Compared to using the Mualem model, both van Genuchten model parameters are different (Table 12). Although not shown here the burn-in period was longer than for the Mualem model, at nearly 5,000 iterations per chain, and the total simulation was 40,050 iterations. The porosity and permeability have similar values, but m and α are quite different between the two relative permeability models.

Table 12. Statistics on posterior distribution for Sample 1, using Burdine relative permeability.

Parameter [units]	Mean	Variance	Mode	Mode w/ all data
Porosity (n) [-]	0.254	2.00×10^{-5}	0.251	0.266
Permeability (k) [m^2]	$10^{-12.95}$	3.31×10^{-3}	$10^{-12.92}$	$10^{-13.21}$
van Genuchten m [-]	0.819	4.02×10^{-3}	0.855	0.398
van Genuchten α [1/Pa]	$10^{-3.53}$	3.12×10^{-3}	$10^{-3.53}$	$10^{-4.00}$

The horsetail plot of model and data (Figure 44) shows the Burdine model can fit the data nearly as well as the Mualem model, with different values for the two-phase parameters. The extrapolation of the mass imbibed from the Burdine model (using both datasets – about 200 g at 10^4 sec) is notably less than the predicted mass imbibed from the Mualem model (Figure 10 – about 250 g at 10^4 sec).

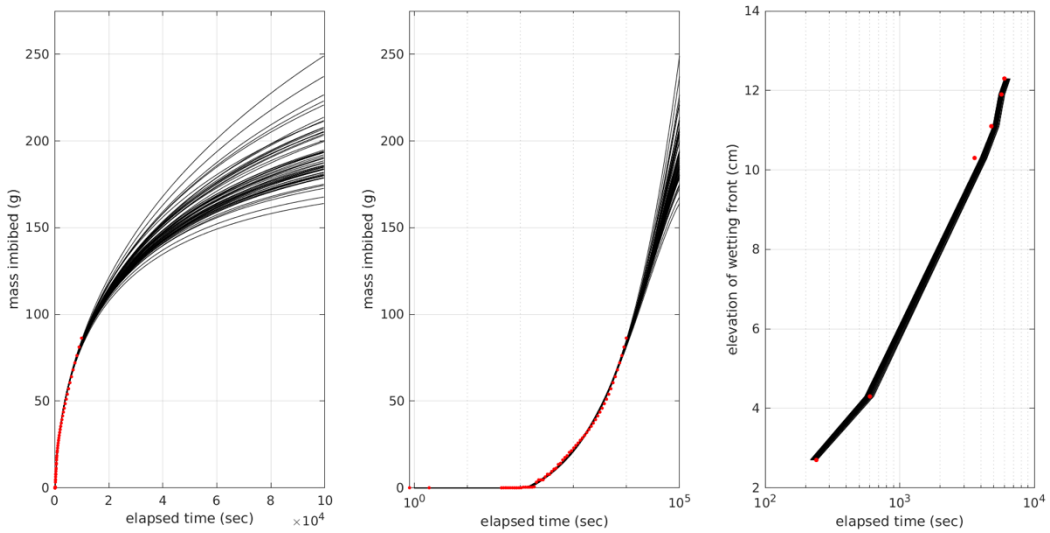

Figure 44. Horsetail plot of 60 models from posterior (black lines) against observations (red dots) for Sample 1, using Burdine relative permeability.

This exercise is done to show the sensitivity of the approach to the form of the relative permeability model. The Mualem and Burdine models present alternative conceptualizations regarding the relation between the relative permeability model and the capillary pressure model (see Figure 2). The Mualem model is more popular than Burdine, but here the two are compared mainly to illustrate that the inverse-modeling method we present here is sensitive to both curves. If the same model is used during parameter estimation and forward model predictions, the choice of model doesn't necessarily matter, but it does impact the estimated parameters, especially m.

The m and α parameters in the Mualem and Burdine relative permeability models have different physical significance, due to the quite different functional forms of equations (5) and (9). The parameters are not expected to have the same values between these two models, but Figure 45 shows that a relatively high-permeability and lower-capillarity Burdine model (blue and green curves) gives similar predictions to a lower-permeability and higher-capillary Mualem model (yellow curves). The user should choose the moisture retention and relative permeability constitutive models for their application based on convenience or physical requirements. Whichever model is needed in the final application should be used in the parameter estimation process.

The data could be fit against a PFLOTRAN simulation using any of a range of different constitutive models, for example the Brooks-Corey exponential (with Mualem or Burdine relative permeability), the linear capillary pressure model, or the extended lognormal Kosugi model (Malama & Kuhlman, 2014). Currently in PFLOTRAN, only the van Genuchten model has been extended to model systems below residual saturation (these optimizations and speed-ups make the parameter estimation process viable), but it is possible this approach could be extended to other two-phase flow constitutive models, allowing similar comparisons.

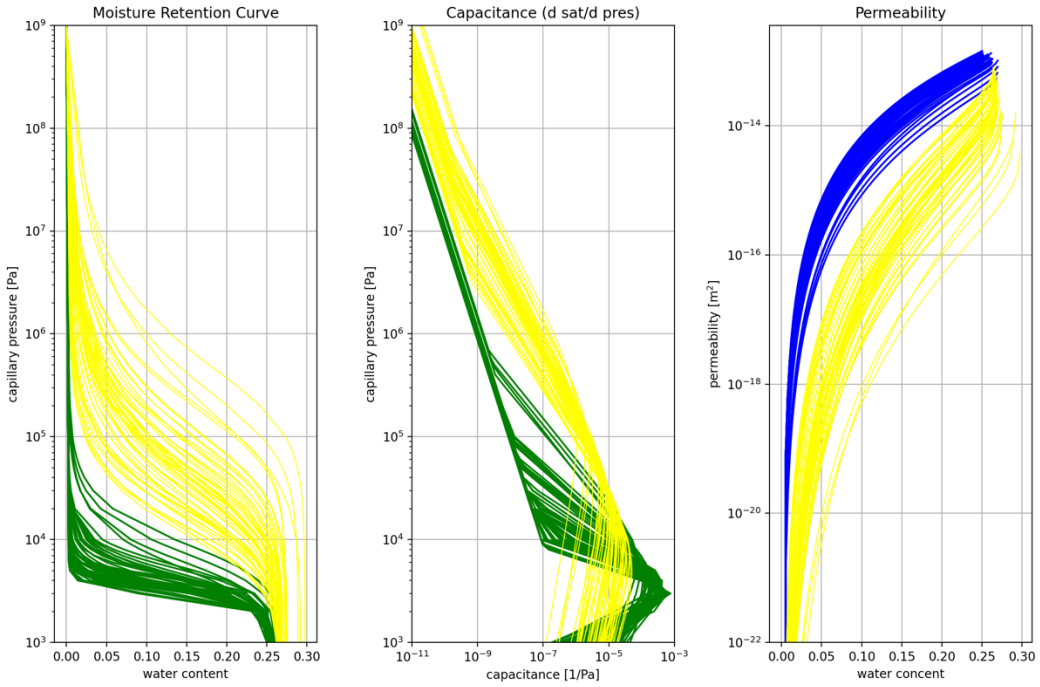

Figure 45. Horsetail of 60 moisture retention, capacitance, and relative permeability curves for Sample 1, using Burdine relative permeability. Yellow curves for Mualem model (Figure 11).

5. SUMMARY AND FUTURE WORK

In summary, the modeling and laboratory method presented here appears to be a simple-to-execute, but promising approach for estimating two-phase flow properties in larger intact samples of volcanic tuff. Compared to mercury injection or classical steady-state infiltration tests, dynamic spontaneous imbibition tests are simpler to run and sensitive to both the moisture retention curve and the relative permeability curve, but more difficult to analyze.

5.1. Experimental Method

We demonstrate the method with four samples of vitric and zeolitized volcanic tuff from the vicinity of P-Tunnel at the NNSS, collected as part of the UNESE project. We were able to get unique parameter fits for three of these samples. The zeolitized non-welded tuff sample was much lower permeability and air-entry pressure (i.e., the wetting front speed was approximately 1000 times slower than the other samples); the test was apparently not capillary dominated.

5.2. Numerical Modeling Method

Especially for samples with van Genuchten m close to unity, the newly developed loop_invariant and unsaturated_extension options in PFLOTRAN were critical in the success of the inversion approach. These options sped up each forward model, sometimes orders of magnitude for certain pathological combinations of parameters (specifically large α and m) which can lead to very high capillary pressures and undefined capacitance (needed during non-linear iteration). The previous implementation of the van Genuchten capillary pressure curve in PFLOTRAN resulted in some forward runs either failing to converge or taking so long to run (e.g., hours per simulation) the MCMC process became infeasible.

5.3. Parameter Estimation Results

We were able to fit numerical models with homogeneous properties to observed time series of water mass imbibed and wetting front elevations (summarized in Table 13). Using MCMC methods, we can see not only the mostly likely parameter estimate associated with each test, but the relative uncertainty in each parameter estimate (see variance in Table 13 or histogram posterior plots), and any strong correlations that exist between parameters from the pairwise posterior plots.

Table 13. Summary of estimated mean parameters (upper row) and their variances (lower row).

Sample	n [-]	k [m^2]	m [-]	α [1/Pa]	Wetting front speed [m/s]
1	0.270	2.95E-14	0.414	4.17E-5	1.87E-5
	7.8E-5	0.15	0.0025	0.0017	
3	0.272	1.62E-16	0.889	9.55E-7	1.41E-5
	2.2E-5	0.29	0.0012	0.29	
4	0.290	2.04E-13	0.954	2.14E-4	6.12E-5
	2.1E-5	0.0017	0.0007	0.0017	

Table 14 summarizes the correlations observed between parameters in their posterior distributions. Across the three samples with good parameter estimates the van Genuchten α and permeability are positively correlated, and porosity was either negatively or not correlated with the other parameters.

Table 14. Summary of inter-parameter correlation in posterior.

	n [-]		k [m^2]		m [-]		α [1/Pa]	
Sample	$-$	$+$	$-$	$+$	$-$	$+$	$-$	$+$
1	k, m, α		n	α	n	α, k	n	k
3	m			α	n			k
4				α, m		k, α		m, k

All the samples showed correlation between the van Genuchten α and permeability. The best-fit linear trend representing $\log_{10}(\alpha) = a \cdot \log_{10}(k) + b$, where a is slope and b is the intercept, for the base-10 log-transformed distributions in the posteriors are given in Table 15. The slopes and intercepts are quite similar for Samples 1 and 3. This relationship indicates, for example, $\alpha = 10^{-6}$ $1/\mathrm{Pa}$ would correspond roughly to $k = 10^{-16}$ m^2. For Sample 4, the slope is similar, but the offset is closer to 9, so $k = 10^{-12}$ would correspond to $\alpha = 10^{-3}$.

The slopes and intercepts are different when only using one of the two datasets or using the Burdine relative permeability model instead of Mualem, but the strong correlation between the parameters remains. The posterior distribution uniquely estimates this relationship at the same time as the best-fit parameters themselves. The estimate of slope is obtained from the entire ensemble (and is valid over a relatively wide range of parameter values), rather than a single perturbation of the model.

Table 15. Slope and intercept for linear relationship between $\log_{10}(\alpha)$ and $\log_{10}(k)$.

Sample	Slope (a)	Intercept (b)
1	1.06	10.0
3	1.00	9.81
4	0.967	8.59
1 (mass only)	0.890	7.87
1 (wetting front only)	0.941	8.30
1 (both w/ Burdine)	0.952	8.79

5.4. Sensitivity and Data Importance

The data importance and sensitivity section illustrated that parameter sensitivity increases with time and the parameters could be estimated from the mass imbibed data alone for Sample 1, but with additional uncertainty in the estimated parameters. Comparing the predictions, it appears the porosity is more constrained by the wetting front elevation data alone, while the permeability is more constrained by the mass imbibed data alone. Only joint inversion with both datasets allows estimation of both van Genuchten parameters.

The parameter estimation done with the Burdine relative permeability model clearly illustrates the estimates of the two-phase flow properties are sensitive to both the moisture retention curve (same between both models) and the relative permeability curve (only difference between Mualem and Burdine). It is up to the user to choose the appropriate constitutive relationship for a problem, but this comparison was done to illustrate how the two are estimated jointly in the proposed approach, rather than simply predicting permeability based on fits of parameters to moisture retention curves.

5.5. Future Work

Based on the initial success of this hybrid experimental and numerical modeling method, we intend to work to further improve both the laboratory apparatus and inverse modeling methods. We will test the method with different types of rocks, including fractured or crushed rocks.

Compared to results obtained in fractured volcanic tuff by Peters et al. (1987), these results correspond to the "early time" results that are associated with an infinite medium (imbibition did not significantly interact with the boundary at the far end of the core). Early-time imbibition data are affiliated with the smallest pore sizes, which fill with water first during imbibition. In follow-on tests we will test both shorter length cores and run longer tests, to observe sample end effects to determine if we can quantify contributions to the two-phase flow properties from larger pores or fractures. These more complex responses could be interpreted with a PFLOTRAN model using a multicontinuum approach (Klavetter & Peters, 1986; Kuhlman & Heath, 2021), using a multi-modal moisture retention curve (Priesack & Durner, 2006), or possibly through some heterogeneous numerical model including individual fractures (Eaton & Bixler, 1987). Further analysis of X-ray CT data may help constrain the relative abundance of sample constituents that may have different capillary and relative permeability characteristics, and petrographic analysis and/or wettability tests may further constrain components that are water sensitive.

The association between the observed wetting front and the point and time in the model when 50% saturation is first crossed is a large simplifying assumption in this analysis, upon which this method relies. When there is a sharp wetting front, a change from dry to "mostly wet" saturation is a valid assumption and should happen at essentially the same time as when the 50% saturation threshold is crossed. Alternative approaches to automate measurement of the wetting front position in the lab and to quantify the wetting front location in the numerical model will be explored. Repeatability of tests on individual cores will be investigated (oven drying samples between tests), as well as the collection of additional data types (e.g., liquid pressure in the sample reservoir) to improve model predictions at early times. We want to make comparisons of the estimated moisture retention curves against other approaches on the same sample. If available, these data could be used in the MCMC parameter estimation process as prior information.

REFERENCES

Adamson, A.W. & A.P Gast, 1997. *Physical Chemistry of Surfaces*, Sixth Edition, Wiley Interscience.

Ankeny, M.D., 1988. *Characterization of Soil Macropores by Infiltration Measurements*, PhD Dissertation, Iowa State University.

Bruce, R.R. & A. Klute, 1956. The measurement of soil moisture diffusivity. *Soil Science Society of America Journal, 20*(4):458-462.

Burdine, N.T., 1953. Relative permeability calculations from pore size distribution data. *Journal of Petroleum Technology, 5*(3):71-78.

Constantz, J. & F. Murphy, 1987. An automated technique for flow measurements from Mariotte reservoirs. *Soil Science Society of America Journal, 51*(1):252-254.

Doherty, J., 2015. *Calibration and Uncertainty Analysis for Complex Environmental Models*, Brisbane, Australia: Watermark Numerical Computing.

Dullien, F.A.L, 1992. *Porous Media: Fluid Transport and Pore Structure*, Second Edition, Academic Press

Eaton, R.R. & N.E. Bixler, 1987. "Analysis of a Multiphase Porous-Flow Imbibition Experiment in Fractured Volcanic Tuff" in Evans, D.D. & T.J. Nicholson [Eds], *Flow and Transport Through Unsaturated Fractured Rock* (pp. 91-97), AGU Monograph 42, Washington, DC: American Geophysical Union.

Haase, R., L.A. Royer, P. Steinbach, D. Schmidt, A. Dibrov, U. Schmidt, M. Weigert, N. Maghelli, P. Tomancak, F. Jug & E.W. Myers, 2020. CLIJ: GPU-accelerated image processing for everyone. *Nature Methods, 17*(1):5–6.

Hammond, G.E., P.C. Lichtner & R.T. Mills, 2014. Evaluating the performance of parallel subsurface simulators: An illustrative example with PFLOTRAN. *Water Resources Research, 50*(1), 208-228.

Heath, J.E., J.E. Bower, J.E. Wilson, K.L. Kuhlman, & S.T. Broome, 2020. X-*ray Computed Tomography on UNESE Core: FY20 Data Report to Support Fracture and Multiphase Fluid Flow Studies*, (18 p.) SAND2020-13578. Albuquerque, NM: Sandia National Laboratories.

Heath, J.E., K.L. Kuhlman, S.T. Broome, J.E. Wilson & B. Malama, 2021. Heterogeneous multiphase flow properties of volcanic rocks and implications for noble gas transport from underground nuclear explosions. *Vadose Zone Journal, 20*(3):e20123.

Hillel, D., 1998. *Environmental Soil Physics*, Academic Press.

Klavetter, E.A. & R.R. Peters, 1986. *Estimation of Hydrologic Properties of an Unsaturated, Fractured Rock Mass*, (53 p.) SAND84-2642. Albuquerque, NM: Sandia National Laboratories.

Kuhlman, K.L. & J.E. Heath, 2021. *Multicontinuum Flow Models for Assessing Two-Phase Flow in Containment Science,* (67 p.) SAND2021-7191. Albuquerque, NM: Sandia National Laboratories.

Kwicklis, E.M., F. Thamir, R.W. Healy & D. Hampson, 1998. *Numerical Simulations of Air- and Water-Flow Experiments in a Block of Variably Saturated, Fractured Tuff from Yucca Mountain, Nevada*, (71 p.) USGS WRIR 97-4274, Denver, CO: US Geological Survey.

Li, K. & R.N. Horne, 2006. Generalized scaling approach for spontaneous imbibition: an analytical model. *SPE Reservoir Evaluation and Engineering, 9*(3):251-258.

Lichtner, P.C., G.E. Hammond, C. Lu, S. Karra, G. Bisht, B. Andre, R.T. Mills, J. Kumar & J.M. Frederick, 2021. *PFLOTRAN Online Theory Guide*, https://www.pflotran.org/documentation/theory_guide/theory_guide.html.

Malama, B. & K.L. Kuhlman, 2015. Unsaturated hydraulic conductivity models based on truncated lognormal pore-size distributions. *Groundwater, 53*(2):498-502.

Mualem, Y., 1976. A new model for predicting the hydraulic conductivity of unsaturated porous media. *Water Resources Research, 12*(3):513-522.

Nole, M., R.C. Leone, H.D. Park, M. Paul, A. Salazar, G.E. Hammond & P.C. Lichtner, 2021. *PFLOTRAN Development FY2021,* (121 p.) SAND2021-8709R, Albuquerque, NM: Sandia National Laboratories.

Peters, R.R., E.A. Klavetter & J.T. George, 1987. "Measuring and Modeling Water Imbibition into Tuff" in Evans, D.D. & T.J. Nicholson [Eds], *Flow and Transport Through Unsaturated Fractured Rock* (pp. 99-106), AGU Monograph 42, Washington, DC: American Geophysical Union.

Priesack, E. & W. Durner, 2006. Closed-form expression for the multi-modal unsaturated conductivity function. *Vadose Zone Journal, 5*:121–124.

Rasmussen, T.C., S.C. Rhodes, A. Guzman & S.P. Neuman, 1996. *Apache Leap Tuff INTRAVAL Experiments*, (108 p.) NUREG/CR-6096, Washington DC: US Nuclear Regulatory Commission.

Richards, L.A., 1931. Capillary conduction of liquids through porous mediums. *Physics, 1*(5):318-333.

Romano, C., J.M. Minto, Z.K. Shipton & R.J. Lunn, 2019. Automated high accuracy, rapid beam hardening correction in X-Ray Computed Tomography of multi-mineral, heterogeneous core samples. *Computers & Geosciences, 131*:144-157.

Sahimi, M., 2011. *Flow and Transport in Porous Media and Fractured Rock*, Second Edition, Wiley-VCH.

Schmid, K.S., N. Alyafei, S. Geiger & M.J. Blunt, 2016. Analytical solutions for spontaneous imbibition: fractional-flow theory and experimental analysis. *SPE Journal, 21*(6):2308-2316.

Schmid, K.S. & S. Geiger, 2012. Universal scaling of spontaneous imbibition for water-wet systems. *Water Resources Research, 48*(3):W03507.

Schindelin, J., I. Arganda-Carreras, E. Frise, V. Kaynig, M. Longair, T. Pietzsch, S. Preibisch, C. Rueden, S. Saalfeld, B. Schmid, J. Tinevez, D.J. White, V. Hartenstein, K. Eliceiri, P. Tomancak & A. Cardona, 2012. Fiji: an open-source platform for biological image analysis. *Nature Methods 9*(7):676–682.

Stephens, D.B., 1996. *Vadose Zone Hydrology*, CRC Press.

Sun, Y., T.A. Buscheck, K.H. Lee, Y. Hao & S.C. James, 2010. Modeling Thermal-Hydrologic Processes for a Heated Fractured Rock System: Impact of a Capillary-Pressure Maximum. *Transport in Porous Media*, 83:501-523.

Tuller, M. & D. Or, 2005. "Water Retention and Characteristic Curve" in Hillel, D. [Ed], *Encyclopedia of Soils in the Environment, Volume 4* (pp. 278-289), Academic Press.

van Genuchten, M.Th., 1980. A closed-form equation for predicting hydraulic conductivity of unsaturated soils. *Soil Science Society of America Journal, 44*(5):892-898.

Vrugt, J.A., 2016. Markov chain Monte Carlo simulation using the DREAM software package: theory, concepts, and MATLAB implementation. *Environmental Modelling & Software, 75*:273-316.

Vrugt, J.A., C.J.F. ter Braak, C.G.H. Diks, B.A. Robinson, J.M. Hyman, & D. Higdon, 2009. Accelerating Markov chain Monte Carlo simulation by differential evolution with self-adaptive randomized subspace sampling. *International Journal of Nonlinear Sciences and Numerical Simulation, 10*(3):273–290.

Warrick, A.W., 2003. *Soil Water Dynamics*, Oxford Press.

Webb, S.W., 2000. A simple extension of two-phase characteristic curves to include the dry region. *Water Resources Research.* 36(6):1423-1430.

Zimmerman, R.W., G.S. Bodvarsson & E.M. Kwicklis, 1990. Absorption of water into porous block of various shapes and sizes, *Water Resources Research, 16*(11):2797-2806.

DISTRIBUTION

Email—Internal

Name	Org.	Sandia Email Address
Technical Library	01977	sanddocs@sandia.gov

This page left blank

This page left blank

Sandia National Laboratories

Sandia National Laboratories is a multimission laboratory managed and operated by National Technology & Engineering Solutions of Sandia LLC, a wholly owned subsidiary of Honeywell International Inc. for the U.S. Department of Energy's National Nuclear Security Administration under contract DE-NA0003525.